Simultaneous development of the hydrodynamic and thermal boundary layers of mixed convective laminar flow through a horizontal tube with a constant heat flux

Marilize Everts[1,*], Mostafa Mahdavi[1], Mohsen Sharifpur[1,2,*] and Josua P. Meyer[1]

[1]Department of Mechanical and Aeronautical Engineering, University of Pretoria, Private Bag X20, Hatfield 0028, Pretoria, South Africa.
[2]Department of Medical Research, China Medical University Hospital, China Medical University, Taichung, Taiwan.
**Corresponding authors email: marilize.everts@up.ac.za (M. Everts)*
and mohsen.sharifpur@up.ac.za (M. Sharifpur)

Abstract

The thermal and hydrodynamic features of developing mixed convective laminar flow in a long horizontal tube were numerically and experimentally investigated. The tube was heated at different constant heat fluxes and had an inner diameter of 11.52 mm and a total length of 9.5 m. Numerical simulations were conducted using ANSYS-Fluent 19.3 with a highly structured mesh and accurate temperature-dependant thermophysical properties for water. The studied parameters consisted of the wall temperatures, Nusselt numbers, vorticity, velocity and temperature gradients, hydrodynamic and thermal boundary layer development, secondary flow, as well as significant momentum terms. By analysing the vorticity characteristics, it was found that our conventional understanding of the merging boundary layer in internal tube flows had to be modified. Subsequently, methods were proposed to determine the development of the hydrodynamic and thermal boundary layers, as well as the momentum terms. The experimental and numerical results indicated that the local mixed convective Nusselt numbers decreased near the tube inlet but then increased along the tube length as secondary flow increased significantly. Furthermore, an increase in secondary flow led to a decreased thermal entrance length but increased hydrodynamic entrance length. By analysing the simultaneous development of the hydrodynamic and thermal boundary layers, it was revealed that the entrance region of a mixed convective laminar flow could be divided into six regions: (1) hydrodynamic inlet region, (2) buoyancy development region, (3) buoyancy dominating region, (4) buoyancy settling region, (5) hydrodynamically stabilising region, and (6) fully developed region.

Keywords: Mixed convection, hydrodynamic boundary layer, thermal boundary layer, boundary layer thickness, simultaneous developing, CFD

Nomenclature

A	Area [m^2]
BPF	Buoyancy and pressure gradient force [N/m^3]
c_p	Specific heat capacity [J/kg.K]
D	Inner diameter [m]
D_o	Outer diameter [m]
EB	Energy balance error [%]
g	Gravitational acceleration [m/s^2]
Gr	Grashof number [-]
Gr^*	Modified Grashof number [-]
Gz	Graetz number
h	Heat transfer coefficient [W/m^2.K]
I	Current [A]
IF	Inertia force [N/m^3]
k	Thermal conductivity [W/m.K]
L	Tube length [m]
$\dot{m}$	Mass flow rate [kg/s]
Nu	Nusselt number [-]
P	Pressure [Pa]
Pr	Prandtl number [-]
$\dot{Q}_e$	Electrical input rate [W]
$\dot{Q}_w$	Water heat transfer rate [W]
$\dot{q}$	Heat flux [W/m^2]
Ra	Rayleigh number
Re	Reynolds number [-]
SFS	Secondary Flow Strength
T	Temperature [°C] or [K]
u, v, w	Fluid velocity in *x*-, *y*- and *z*- directions [m/s]
V	Voltage [V]
VF	Viscous force [N/m^3]
x, y	Cross-sectional positions [m]
z	Axial position along tube length [m]

Greek letters

β	Expansion coefficient [1/K]
μ	Viscosity [Pa.s]
ψ	Stream function [m^2/s]
$\emptyset$	Computational cell variable
ρ	Density [kg/m^3]
ρ_0	Density at reference temperature [kg/m^3]
v	Kinematic viscosity [m^2/s]

Subscripts

b	Fluid bulk
i	Tube inlet
m	Mean
o	Tube outlet
s	Tube inner surface

1 Introduction

Heat transfer and thermal diffusion are commonly found in industrial processes using internal flows. The induced heat on the tube surfaces often leads to buoyancy effects, due to the fluid density being dependent on temperature, which increases the heat transfer rate [1]. In their extensive experimental study, Meyer and Everts [2] concluded that due to these temperature and density differences inside the tube in the presence of gravity, mixed convective flow exists in the majority of the heat exchangers, while forced convective flow seldom occurs. Over the past century, the mixed convective flow has been extensively investigated [3] and reviewed in book chapters [4, 5] and review articles [6-8]. Previous studies also investigated the fundamental aspects of mixed convective developing and fully developed flow through tubes [2, 9-12]. For tubes heated at a constant heat flux, these sources indicate that extensive research was conducted between the 1950s and 1990s. During the last decade, the focus has shifted to areas such as particulate systems of mixed convective flow [13].

Due to the advantage of the improved heat transfer that buoyancy effects can contribute, attention has been given to the influence of buoyancy effects on the laminar Nusselt numbers, especially for fully developed flow. For developing flow, Oliver [1] notes that formulising the Nusselt number in mixed convection can be, to some extent, inaccurate and conditional correlations can be proposed. Similarly, McComas and Eckert [14] emphasise the challenge of correlating the local Nusselt numbers in the entrance region due to the significant impacts of the onset of natural convection.

Shannon and Depew [15] measured a section of a horizontal tube where the fully developed flow was hydrodynamically achieved while the flow was thermally developing. An unusual heat transfer trend was observed with the presence of a trough in the local Nusselt numbers. The authors briefly mentioned that free convection effects were possibly the reason for the pattern. The same trend in the local Nusselt numbers was found by other authors who investigated mixed convective flow through horizontal tubes [2, 16-19].

Bergles and Simonds [20] point out that the geometry and material of the tubes can noticeably change the Nusselt numbers of mixed convective flow. However, they did not report any unusual Nusselt number trends. Piva *et al*. [19] propose the same idea, stating that the wall conductivity can contribute to the pressure drop. They also mention that the wall thermal conductivity can be a contributing factor in the decreasing and then increasing trends of the local Nusselt numbers, while the axial conduction may play a noticeable role in the final rise of the local Nusselt numbers after its minimum value.

Meyer et al. [21] investigated mixed convective flow in horizontal, inclined and vertical tubes and found that buoyancy effects decreased with increasing inclination angles. For vertical flow, buoyancy effects were suppressed and forced convection conditions existed. In a follow-up study, Everts et al. [22] confirmed that buoyancy effects were suppressed for Reynolds numbers greater than 600, but reported that opposing and assisting flow became significant at lower Reynolds numbers. These studies focused mainly on fully developed flow and not necessarily the development of the heat transfer coefficients in forced and mixed convective flow.

Cheng and Ou [17] observed three regions, containing unique heat transfer mechanisms, in the local Nusselt numbers. In the Leveque solution region, the buoyancy effects of convective terms were negligible compared with the axial convective term, and the local Nusselt numbers decreased with the axial position. The authors explained that once the free convection and entrance effects were balanced, a minimum Nusselt number was reached. In the intermediate region, buoyancy effects were significant and led to increasing local Nusselt numbers along the tube length. After that, the local Nusselt numbers decreased to an asymptotic value in region 3.

Meyer and Everts [2] carried out an extensive study on the local heat transfer characteristics of forced and mixed convective developing flow. Similar to Cheng and Ou [17], they identified and quantified (by developing correlations) three distinct regions for mixed convective flow. The study of Meyer and Everts [2] was experimental, and although it was not possible for them to experimentally investigate the thermal boundary layer, they postulated from the Nusselt number behaviour as a function of tube length that the three distinct laminar regions occurred due to the development of the thermal boundary layer. The authors explained that the increasing thermal boundary layer thickness causes the decreasing local Nusselt numbers in the forced convection developing (FCD) region. However, buoyancy effects were suppressed in this region due to the thin thermal boundary layer thickness. Buoyancy effects were significant in the mixed convection developing (MCD) region, and increased with the increasing thermal boundary layer thickness along the tube length. This enhanced the heat transfer inside the tube and caused the local Nusselt numbers to increase. In the fully developed (FD) region, the buoyancy effects and Nusselt numbers remained constant due to the thermal boundary layer thickness being constant.

Most of the theoretical analyses of mixed convective flow were conducted before the year 2000 [23-27], and even for tube flows [19, 28-31]. Looking at the governing equations of laminar mixed convective flow, the equations can be summarised as continuity, momentum and energy with the inclusion of the buoyancy term. The complexities are revealed when, regardless of laminar forced convective flow, the presence of most of the terms is essential for analytical or numerical simulations. This explains why many textbooks only briefly considered this specific field [32-35]. Similarity solutions and different analytical methods were described in detail in the textbook by Shang and Zhong [36], which is one of the very few textbooks dealing particularly with mixed convection.

Shannon and Depew [30] conducted one of the first numerical investigations for laminar flow, specifically for Reynolds numbers below 300. For simplicity, the axial and radial conduction, as well as buoyancy terms were ignored. It was found that the results could be negatively affected when $Ra^{0.25}/NuGz > 2$, indicating the importance of the buoyancy term. Furthermore, the authors found it necessary to make use of temperature-dependent viscosity in the findings.

Newell and Bergles [31] developed a differential formulation to solve the secondary flow field in polar coordinates in specific cross-sections. The equations were non-dimensionalised using the stream functions, and the finite difference method was employed. The thermal boundary conditions were limited to two extreme wall conditions: one using a glass tube with a thermal conductivity close to the fluid, and the other using a tube with an infinite thermal conductivity. To some extent, Muzzio and Parolini [28] utilised a similar model of equations that could capture the secondary flow in the tube cross-section appropriately.

Hong and Bergles [29] used the integral analytical method to solve a two-dimensional cross-section of a horizontal tube for mixed convective flow, focusing on developing correlations for average Nusselt numbers. Using computational fluid dynamics (CFD) with control volume discretisations of variables and the SIMPLE scheme, Piva *et al*. [19] found that the numerical results were in good agreement with most of the experimental results. Unfortunately, only the Nusselt numbers and surface temperatures from the CFD analysis were published, and no further evidence was presented to support how buoyancy effects changed the local Nusselt number trends.

Although mixed convective flow has been investigated experimentally, analytically and numerically in the past, the previous studies focused mainly on reporting the local Nusselt numbers and temperature profiles. Furthermore, most studies were conducted when there were limited computational facilities to solve large CFD grids. Thanks to the enhancement of CFD capabilities, laminar mixed convective flow in a long horizontal tube was investigated in this paper. This has not been done before. Previous studies, before the work of Meyer and Everts [2], were limited to length-to-diameter ratios of 640 [15], while the majority of investigations were conducted using tubes with length-to-diameter ratios between 30 [37] and 120 [38]. In this paper, the length-to-diameter ratio is 828, which reveals new original perspectives.

Therefore, this paper aims to present the results of both the hydrodynamic and thermal boundary layer development by implementing novel approaches. Furthermore, the reasons for the changes in heat transfer characteristics of mixed convective flow, compared with the forced convective flow, are explained in this study. These results contribute to improving our fundamental understanding of the influence of the buoyancy effects on the flow development along the tube. It will also assist in determining to what extent the developing flow will have an effect on the overall pressure drop and heat transfer inside the heat exchanger.

2 Experimental setup

The experimental setup and procedure, as well as the instrumentation preparation, installation and calibration, are fully reported in Meyer and Everts [2] and Everts and Meyer [39] and only summarised in this paper. The experimental setup (Figure 1) consisted of a closed-loop fluid system which circulated the test fluid from a storage tank through a flow-calming section, inlet section, test section and mixer, and back to the storage tank.

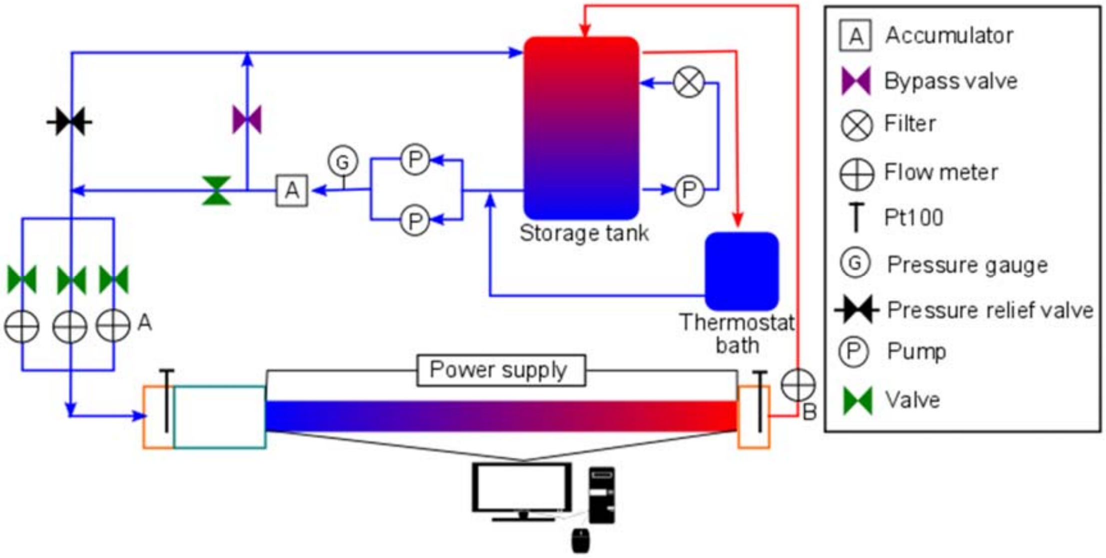

Figure 1: Schematic of the experimental setup used to conduct the heat transfer measurements.

The copper test section (Figure 2) had an inner diameter, an outer diameter, and a length of 11.52 mm, 12.7 mm, and 9.81 m, respectively. T-type thermocouples were soldered onto the test section and calibrated in situ between 20 and 60 °C, to an accuracy of 0.1 °C. Constant heat flux was applied by coiling four constantan wires (connected in parallel) around the test section.

The test section was thermally insulated with 120 mm-thick Armaflex insulation (thermal conductivity of 0.034 W/m.K). The lab was temperature-controlled (24/7) to a constant temperature of 21.8 °C which made it possible to conduct experiments at constant ambient conditions. Due to the constant heat flux boundary condition that was applied to the test section, the surface temperatures increased along the tube length. To minimise heat losses, the inlet temperature was chosen to be close to the ambient temperature. Therefore, the maximum heat losses can be expected near the outlet of the test section, while the heat losses near the inlet of the test section was negligible. One-dimensional conduction heat transfer calculations estimated the maximum heat loss to be less than 3%, and axial heat conduction was considered negligible using Maranzana et al. criteria [40].

A flow-calming section was installed upstream of the test section to straighten the flow and ensure a uniform velocity profile at the inlet of the test section. The flow-calming section was manufactured from clear acrylic plastic to ensure that entrained air bubbles could be detected. To prevent any temperature gradients inside the flow-calming section, the fluid first flowed through a 100 mm cavity filled with a soft nylon mesh, before it reached a Pt100 probe, where the average inlet temperature was measured. Thereafter, the fluid passed through several flow straighteners such as perforated acryclic plates with an open-area ratio (OAR) of 0.299, tightly packed soda straws (inside diameter 5.1 mm, length 102 mm, OAR of 0.855), and galvanised steel meshes (wire diameter 0.37 mm, OAR of 0.588). An acetal disc was bolted to the flow-calming section to obtain a square-edged inlet. A bleed valve was installed prior to the inlet section to bleed air that entered the flow-calming section. The Pt100 probe connection inside the flow-calming section was used as another bleed valve. The flow-calming section was properly insulated against heat loss using 40 mm thick insulation with a thermal conductivity of 0.034 W/m.K.

During laminar flow measurements, significant cross-sectional temperature gradients in the radial and tangential directions developed throughout the test section. Therefore, to obtain a uniform outlet temperature, a mixer was added after the test section. The purpose of the mixer was two-fold: to house the splitter plates and to house a Pt100 probe, which was used to measure the outlet temperature. The mixer design was based on work done by Bakker et al. [41], who investigated laminar flow in static mixers with helical splitter plates. The mixer consisted of four copper splitter plates, with a length-to-diameter ratio of 1.5. The elements were positioned and soldered such that the leading edge of an element was perpendicular to the trailing edge of the next element. Every splitter plate repeatedly split the thermal boundary layers to ensure a uniform temperature gradient in the radial direction. The splitter plates were placed inside the acetal mixer, which directed the fluid to flow over and along the Pt100 probe after it has been mixed. This ensured that the entire Pt100 probe was exposed to the mixed fluid and also eliminated any stagnant recirculation zones. The mixer was insulated with 75 mm thick insulation to prevent any heat loss, and air was bled from the mixer using the Pt100 probe connection to the mixer housing.

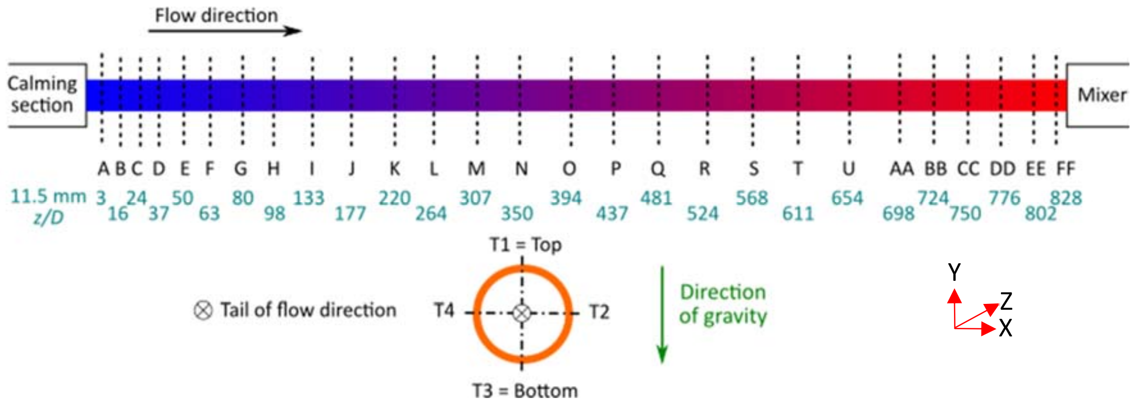

Figure 2: Schematic of the test section indicating the 27 thermocouple stations, A to FF, as well as their axial positions. A cross-sectional view of the test section illustrates the peripheral positions of the four thermocouples.

3 Formulation and numerical method

3.1 Equations

Laminar fluid flow in a circular tube, with dimensions similar to the experimental study (Figure 2), was numerically solved using ANSYS Fluent 19.3. The flow was assumed to be steady, incompressible, single-phase, Newtonian, laminar, without viscous energy dissipations, and with gravity's impact as a body force. The 3D form of the continuity, momentum and energy equations for laminar convective flow was therefore simplified as:

$$\frac{\partial \rho u}{\partial x}+\frac{\partial \rho v}{\partial y}+\frac{\partial \rho w}{\partial z}=0 \tag{1}$$

$$\rho\left(u\frac{\partial u}{\partial x}+v\frac{\partial u}{\partial y}+w\frac{\partial u}{\partial z}\right)= -\frac{\partial P}{\partial x}+2\frac{\partial}{\partial x}\left(\mu\frac{\partial u}{\partial x}\right)+\frac{\partial}{\partial y}\left(\mu\left[\frac{\partial u}{\partial y}+\frac{\partial v}{\partial x}\right]\right)+\frac{\partial}{\partial z}\left(\mu\left[\frac{\partial u}{\partial z}+\frac{\partial w}{\partial x}\right]\right) \tag{2}$$

$$\begin{aligned}\rho\left(u\frac{\partial v}{\partial x}+v\frac{\partial v}{\partial y}+w\frac{\partial v}{\partial z}\right)&= -\frac{\partial P}{\partial y}+\frac{\partial}{\partial x}\left(\mu\left[\frac{\partial u}{\partial y}+\frac{\partial v}{\partial x}\right]\right)+2\frac{\partial}{\partial y}\left(\mu\frac{\partial v}{\partial y}\right)+\frac{\partial}{\partial z}\left(\mu\left[\frac{\partial v}{\partial z}+\frac{\partial w}{\partial y}\right]\right)\\&\quad+(\rho_0-\rho)g\end{aligned} \tag{3}$$

$$\rho\left(u\frac{\partial w}{\partial x}+v\frac{\partial w}{\partial y}+w\frac{\partial w}{\partial z}\right)= -\frac{\partial P}{\partial z}+\frac{\partial}{\partial x}\left(\mu\left[\frac{\partial u}{\partial z}+\frac{\partial w}{\partial x}\right]\right)+\frac{\partial}{\partial y}\left(\mu\left[\frac{\partial v}{\partial z}+\frac{\partial w}{\partial y}\right]\right)+2\frac{\partial}{\partial z}\left(\mu\frac{\partial w}{\partial z}\right) \tag{4}$$

$$\rho c_p\left(u\frac{\partial T}{\partial x}+v\frac{\partial T}{\partial y}+w\frac{\partial T}{\partial z}\right)=\frac{\partial}{\partial x}\left(k\frac{\partial T}{\partial x}\right)+\frac{\partial}{\partial y}\left(k\frac{\partial T}{\partial y}\right)+\frac{\partial}{\partial z}\left(k\frac{\partial T}{\partial z}\right) \tag{5}$$

According to the tube orientation in the computational domain (*x*, *y* and *z* directions shown in Figure 3), *u* and *v* represented the fluid velocities at the tube cross-section and *w* the axial velocity in the *z*-direction. The fluid properties were evaluated at the local fluid temperatures and ρ_0 at the reference temperature which was flow inlet temperature. The fluid properties were evaluated at the local fluid temperatures. Because the fluid properties varied with temperature, the thermophysical correlations of Popiel and Wojtkowiak [42] were used to calculate the density (ρ), dynamic viscosity (μ), thermal conductivity (k) and specific heat (c_p) as a function of temperature [°C]:

$$\rho = a + bT + cT^2 + dT^{2.5} + eT^3 \tag{6}$$

where a = 999.79684, b = 0.068317355, c = -0.010740248, d = 0.00082140905, and e = -2.3030988×10^{-5}

$$\mu=\frac{1}{a+bT+cT^2+dT^3} \tag{7}$$

where a = 557.82468, b = 19.408782, c = 0.1360459, and d = -3.1160832×10^{-4}

$$k = a + bT + cT^{1.5} + dT^2 + eT^{0.5} \tag{8}$$

where a = 0.5650285, b = 0.0026363895, c = -0.00012516934, d = -1.5154918×10^{-6}, and e = -0.0009412945

$$c_p = a + bT + cT^{1.5} + dT^2 + eT^{2.5} \tag{9}$$

where a = 4.2174356, b = -0.0056181625, c = 0.0012992528, d = -0.00011535353, and e = 4.14964×10^{-6}

The Boussinesq approximation, which assumes that the density in the *y*-direction is a linear function [43], is the conventional method for solving the buoyancy term in the momentum equation. However, a third-order polynomial correlation for density was used to improve the accuracy of the calculation in all directions.

The boundary conditions at the tube inlet ($z = 0$) were zero values for the *u*- and *v*-velocities as the flow in the experimental setup entered from a flow-calming section which straightened the flow. The inlet temperature, *T*, and axial velocity, *w*, were uniform and corresponded to the values for the different case studies (three different fluids, three heat fluxes and four Reynolds numbers) with detail specified in the test matrix in Table 1. The case studies corresponded to the experimental data from previous works [2, 10, 12, 44]. A no-slip boundary condition was assumed on the inner wall and a constant heat flux was prescribed with values for the different case studies, as summarised in Table 1. The boundary condition at the tube outlet was prescribed as a fully developed flow, assuming zero gradient of velocity and temperature in the flow direction and thus $\partial u/\partial z = 0$, $\partial v/\partial z = 0$, $\partial w/\partial z = 0$, $\partial T/\partial z = 0$. Everts and Meyer's experiments [11] confirmed this is a valid assumption, due to the long length of the tube. The following schemes were used to solve the governing equations: SIMPLE algorithm, PRESTO! for pressure, and second-order upwind to discretise the momentum and energy terms.

The streamlines (ψ) represent the path of a fluid element tangent to the velocity vector. At each cross-section, only *x*- and *y*-directions were considered, and the streamlines were defined as:

$$\begin{cases} u = \dfrac{\partial \psi}{\partial y} \\ v = -\dfrac{\partial \psi}{\partial x} \end{cases} \tag{10}$$

3.2 Mesh independence study

Four highly structured meshes with appropriate uniformity, similar to the mesh in Figure 3, were generated on the tube's cross-section and evaluated. Although the geometry considered of a smooth circular tube, the high aspect ratio (828) of the tube length (9.5 m) to diameter (0.00115 m) requires a relatively large mesh. The meshes varied in size from 145 000 to 5 230 000 cells. The meshes were highly structured, with appropriate uniformity generated on the tube’s cross-section. At the tube inlet, where the velocity and temperature gradients were the highest, the meshes were closely spaced. Since the flow is laminar, no boundary layer mesh was generated. However, a specific meshing technique was used to ensure higher uniformity of structured mesh at the cross section by creating a square at the middle and generating mesh around it. The spacing was smaller closer to the centre of the tube to maintain the uniformity in most of the cross section. The grid sizes in the radial and tangential direction were 0.0003 m and 0.0009 m, respectively. In the flow direction, a bias factor was used to stretch the grid from the inlet to the outlet, being the same size as the tangential grid at the inlet. The minimum and maximum grid spacing in the flow direction were 0.001 m and 0.01 m, respectively.

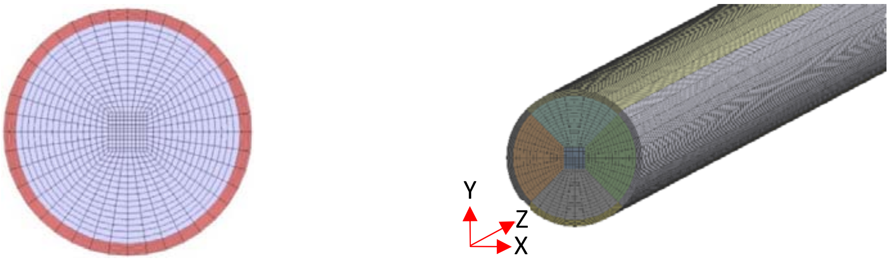

(a) (b)

Figure 3: Structured mesh generation at a) the cross-section of the tube and b) along the axial length of the tube.

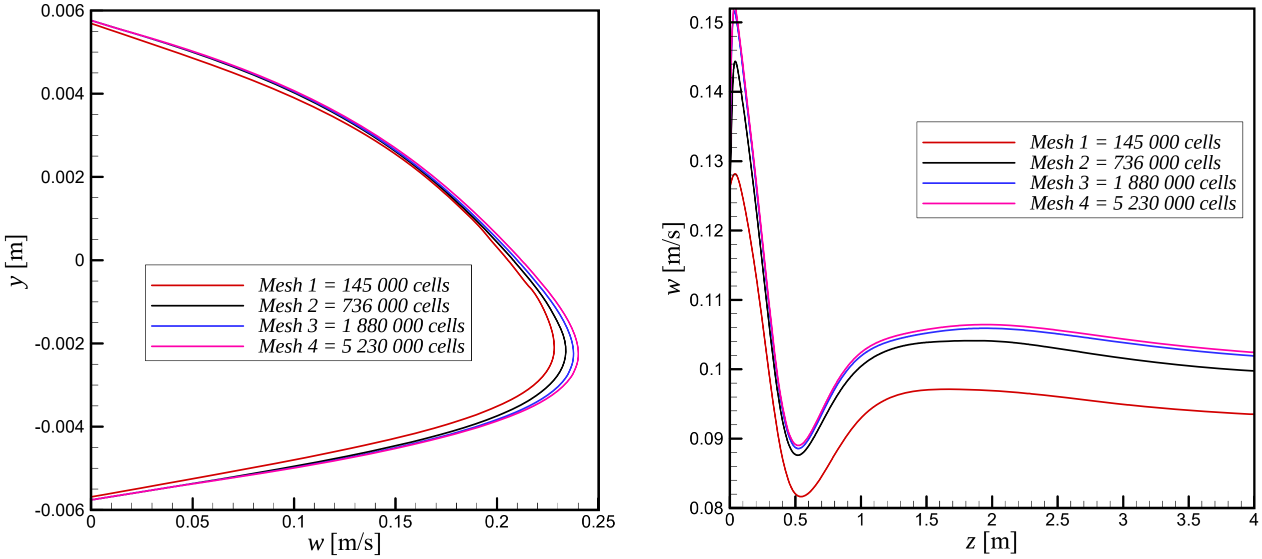

(a) (b)

Figure 4: Mesh independence study for mixed convection conditions by comparing (a) the velocity profile at z = 1 m and (b) the development of the velocity along the tube length close to the tube wall at y = 0.00576 m, Reynolds number of 1 800 and Grashof number of 3.35×10^4.

Two steps were taken to ensure that the mesh was sufficient to produce accurate results: (1) local variables such as the velocity profile, and (2) the local Nusselt numbers and temperatures of the numerical results were compared with the experimental results (Section 8). The velocity profiles at a Reynolds number of 1 800 and heat flux of 3 kW/m^2 (Grashof number of 3.35×10^4) were quantitatively compared for four meshes to examine the generated mesh in the cross-sectional and axial directions. Figure 4(a) compares the velocity in the vertical direction (y) at z = 1 m and Figure 4(b) the velocity in the axial direction at a point close to the top surface (y = 0.00576 m). Although the difference between the velocity profiles of Meshes 1 and 2 was not significant in Figure 4(a), it became prominent in Figure 4(b). Due to the negligible improvement in Meshes 3 to 4 in Figure 4, Mesh 3 (with 1 880 000 cells) was considered the optimal and suitable mesh for this study.

4 Experimental and numerical test matrix

Table 1 summarises the boundary conditions and test matrix of the experiments and numerical simulations conducted at different heat fluxes and Reynolds numbers.

Table 1: Test matrix of experiments and numerical simulations.

Heat flux [kW/m^2]	Reynolds number	Mass flow rate [kg/s]	Inlet temperature [°C]	Grashof number	Prandtl number
3	1 800	0.0128	20.4	3.35×10^4	5.6
1	1 800	0.0151	20.4	8.73×10^3	6.4
1	1 000	0.008	20.4	1.04×10^4	6.0
3	1 000	0.0064	20.4	5.47×10^4	4.9

5 Data reduction

The data reduction method is fully reported in Meyer and Everts [2], but it is summarised in this paper for the sake of completeness. The mean fluid temperature, T_m, at a specific tube location, z, was obtained using a linear temperature distribution:

$$T_m = \left(\frac{T_o - T_i}{L}\right) z + T_i \tag{11}$$

The bulk fluid temperature, T_b, was the average of the inlet, T_i, and outlet, T_o, fluid temperatures:

$$T_b = \frac{T_i + T_o}{2} \tag{12}$$

The average and local fluid properties were determined using the thermophysical correlations for water [42] at the bulk (Eq. (12)) and mean fluid temperatures (Eq. (11)), respectively.

The Reynolds number, Re, was calculated as follows:

$$Re = \frac{\dot{m}D}{\mu A_c} \tag{13}$$

where $\dot{m}$ is the measured mass flow rate, D is the measured inner diameter, μ is the dynamic viscosity, and A_c is the cross-sectional area of the test section ($A_c = \pi/4D^2$).

The heat transfer rate to the water, $\dot{Q}_w$, and heat flux, $\dot{q}$, were determined as:

$$\dot{Q}_w = \dot{m}c_p(T_o - T_i) \tag{14}$$

$$\dot{q} = \frac{\dot{Q}_w}{A_s} = \frac{\dot{m}c_p(T_o - T_i)}{\pi DL} \tag{15}$$

The heat transfer rate to the water, $\dot{Q}_w$, was monitored by comparing it with the electrical input rate, $\dot{Q}_e$, which ideally should be equal because the test section is well insulated. The energy balance error, EB, which ideally should be as close as possible to zero, was determined as follows:

$$EB = \left|\frac{\dot{Q}_e - \dot{Q}_w}{\dot{Q}_e}\right| \times 100 = \left|\frac{\Delta VI - \dot{m}c_p(T_o - T_i)}{\Delta VI}\right| \times 100 \tag{16}$$

The average energy balance error of all the experiments conducted was less than 3%, which was in positive agreement with the calculations for the estimation of the heat losses to the surroundings through the insulation material. As the energy balance was not zero, and some losses did occur to the ambient air, the electrical input rate was always slightly higher than the heat transfer rate to the water. Therefore, the heat transfer rate to the water was used to determine the heat flux (Eq. (15)), since it was regarded as more accurate than the electrical input rate.

As the thermal resistance across the tube wall was found to be negligible, the temperatures on the inner and outer surfaces of the test section were assumed to be equal. Therefore, the average of the four temperature measurements at a station was used as the average inner surface temperature, T_s, at a specific thermocouple station:

$$T_s = \frac{T_1 + T_2 + T_3 + T_4}{4} \tag{17}$$

As the heat flux, $\dot{q}$, surface temperature, T_s, and mean fluid temperature, T_m, were then known, the heat transfer coefficients, h, were determined as follows:

$$h = \frac{\dot{q}}{(T_s - T_m)} \tag{18}$$

The Nusselt numbers, Nu, were determined from the heat transfer coefficients:

$$Nu = \frac{hD}{k} \tag{19}$$

The Grashof numbers, Gr, and modified Grashof numbers, Gr*, were determined by:

$$Gr = \frac{g\beta(T_s - T_m)D^3}{\nu^2} \tag{20}$$

$$Gr^* = GrNu = \frac{g\beta\dot{q}D^4}{\nu^2 k} \tag{21}$$

where the gravitational acceleration, g, was set to 9.81 $\mathrm{m/s^2}$, and the kinematic viscosity was obtained from the density and dynamic viscosity ($\nu = \mu/\rho$).

All uncertainties were calculated within a 95% confidence interval, and the uncertainty analysis details are provided in Everts [44] and Everts and Meyer [39]. The uncertainties of the Reynolds number were approximately 1.5% for all Reynolds numbers, while the mixed convection Nusselt number uncertainties were less than 5% and decreased with increasing heat flux.

6 Method of obtaining the hydrodynamic and thermal boundary layers

To obtain the thickness of the hydrodynamic and thermal boundary layers in the entrance region of a tube, innovative approaches were implemented. The tube's central vertical plane was considered a symmetry plane; therefore, all the proposed parameters and methods were extracted from this plane. This also made it possible to illustrate the boundary layer growth in a two-dimensional graph. The following criteria (graphically summarised in Figure 5) were used to locate the thickness of the boundary layers for mixed convection conditions:

1. It was observed from the simulation results that the core region contained parallel flow before the boundary layer merged. Because the velocity gradient in the y-direction, $\partial w/\partial y$, was approximately zero in this region, the inviscid core region is represented by a flat gradient. The velocity gradient in the y-direction changed at the edge of the hydrodynamic boundary layer. In general, the magnitude of the velocity gradient in the y-direction decreased linearly from the surface to the centre of the tube. Therefore, the hydrodynamic boundary layer thickness after the boundary layer merged corresponded to the minimum value of $|\partial w/\partial y|$, where w is the velocity in the z-direction.

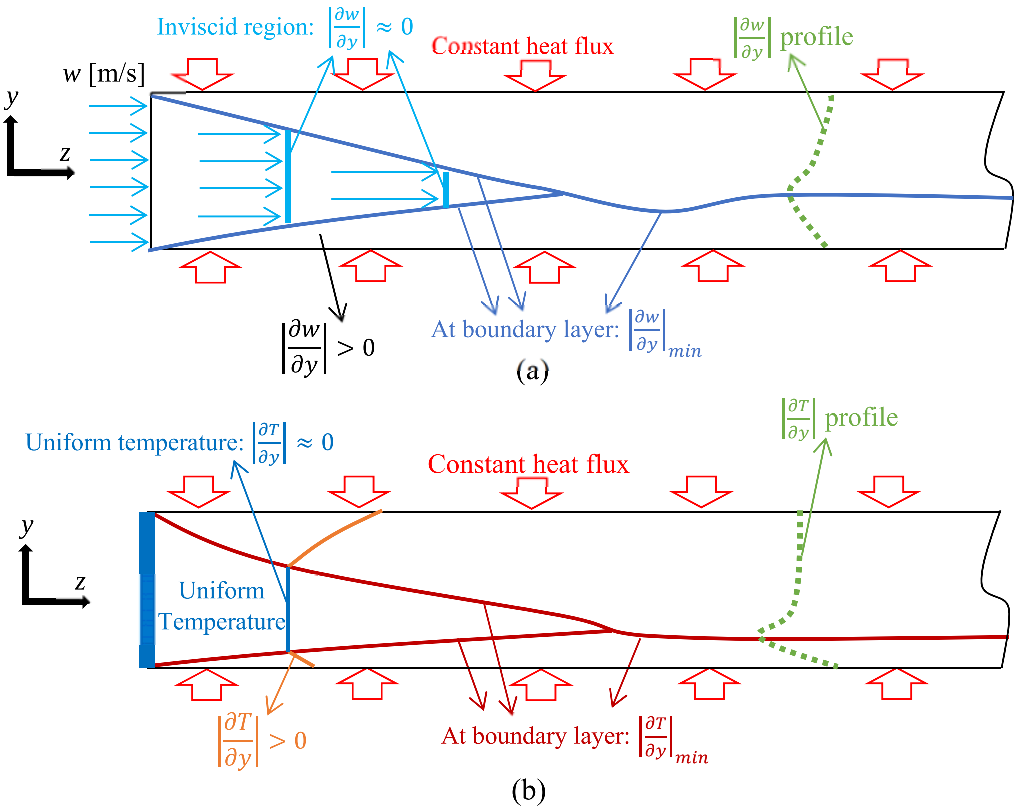

Figure 5: Schematic summary of the criteria used to determine the growth of (a) the hydrodynamic and (b) the thermal boundary layers along the tube length for mixed convection conditions.

2. A similar approach was used to obtain the thermal boundary layer. It was observed from the simulation results that the core region was not affected by the diffusion of the heat flux from the surface before the thermal boundary layer merged. Therefore, the core region had a uniform temperature and zero temperature gradient, $\partial T/\partial y$. The temperature gradient in the y-direction only changed at the edge of the thermal boundary layer. The temperature gradient decreased parabolically from the surface to the centre of the tube and the thermal boundary layer thickness corresponding to the minimum value of the temperature gradient in the y-direction ($|\partial T/\partial y|$).
3. Vorticity, $\nabla \times \vec{u}$, can be used to quantify the rotation of a fluid element due to the shear stress applied on the side faces of each element:

$$\nabla \times \vec{u} = \left(\frac{\partial w}{\partial y} - \frac{\partial v}{\partial z}, \frac{\partial u}{\partial z} - \frac{\partial w}{\partial x}, \frac{\partial v}{\partial x} - \frac{\partial u}{\partial y}\right) \tag{22}$$

   The vorticity magnitude was calculated on the symmetrical plane and plotted along the tube length. Section 9.2 shows that the hydrodynamic boundary layer filled the entire cross-section and merged at the axial position where the vorticity magnitude increased significantly. Before the hydrodynamic boundary layer merged, the vorticity magnitude was approximately zero.
4. According to the thermal boundary layer theory in tube flows, the radial temperature gradient in each cross-section can be assumed to be approximately zero in the inviscid part of the entrance region, while the gradient is more parabolic in the viscous part. Three-dimensional models were solved in Cartesian coordinates in ANSYS Fluent, while the radial temperature gradient had to be calculated in a polar system (not cylindrical) for boundary layer purposes. Therefore, the radial gradient was obtained by using the chain rule:

$$\frac{\partial T}{\partial r} = \frac{\partial T}{\partial x}\frac{\partial x}{\partial r} + \frac{\partial T}{\partial y}\frac{\partial y}{\partial r} \tag{23}$$

$$x = r\cos\theta, \qquad y = r\sin\theta \tag{24}$$

$$\frac{\partial T}{\partial r} = \frac{\partial T}{\partial x}\left[\cos\left(\arctan\left(\frac{y}{x}\right)\right)\right] + \frac{\partial T}{\partial y}\left[\sin\left(\arctan\left(\frac{y}{x}\right)\right)\right] \tag{25}$$

An iso-surface of the temperature gradient, with a reasonably small value, was tracked from the inlet to obtain the three-dimensional boundary layer. Different values were considered, and reasonable results were obtained using $\partial T/\partial r = 5$ K/m. Although the accuracy of the three-dimensional boundary layer is less than when using the vertical symmetrical plane, it provides a better visual understanding of the thermal boundary layer development.

7 Method of obtaining the forces in boundary layers

By investigating the development of the momentum terms inside the boundary layer, valuable insights into mixed convection behaviour can be obtained. The momentum equation usually consists of four major terms: (1) inertia, (2) pressure gradient, (3) buoyancy and (4) viscous. Buoyancy depends on the density and increases linearly with temperature. Furthermore, both mathematically and using CFD calculations, the pressure gradient and buoyancy are found to be in the same order of magnitude, $\frac{\partial P}{\partial Y} \sim \frac{\partial}{\partial Y}(\rho g Y) \sim \rho g$. The only difference is that they act in opposite directions due to the negative sign of the pressure gradient in the momentum equation. Because of this similarity, these two terms were combined and presented with the other terms as three volumetric forces, namely the inertia force (*IF*), buoyancy and pressure gradient force (*BPF*) and viscous force (*VF*):

$$IF = \rho\left(u\frac{\partial v}{\partial x} + v\frac{\partial v}{\partial y} + w\frac{\partial v}{\partial z}\right) \tag{26}$$

$$BPF = -\frac{\partial P}{\partial y} + (\rho_0 - \rho)g \tag{27}$$

$$VF = \mu\left(\frac{\partial^2 v}{\partial x^2} + \frac{\partial^2 v}{\partial y^2} + \frac{\partial^2 v}{\partial z^2}\right) \tag{28}$$

Because buoyancy is only present in the *y*-direction of the momentum equation, terms in this direction only were evaluated. The momentum terms were separated appropriately according to the logical meaning of the forces. The cross-derivative terms in the momentum equations were evaluated and found to be negligible in comparison to the diagonal shear stress terms, therefore Eq. (28) was used as the representative viscous force. The inertia force and the combined buoyancy and pressure gradient force were defined as custom field functions in ANSYS-Fluent for the entire flow field (1 045 000 computational cells). The viscous force was defined as a user-defined function, initially as a first derivative and saved in a user-defined scalar, then as a second derivative with another user-defined memory, before being interpreted in Fluent over the same flow field. The velocity gradients in all three directions were saved using three user-defined scalars. Each gradient was then differentiated and saved in three user-defined memories.

The viscous force was calculated based on these user-defined memories, and the data were extracted as an Excel file to calculate the average force over any differential increment at each cross-section. The volume-weighted averages of the forces in the boundary layer was used as it was found that repeatable and insightful trends in terms of the significance of the different forces in the boundary layer development could be obtained using this approach. For flow through a tube, the hydrodynamic boundary layer developed in three directions; therefore, the average of each force was calculated in each cross-section in the axial direction. For comparison purposes, it was helpful to use normalised values according to their highest quantities ($\frac{\emptyset_{ave}}{\emptyset_{ave-max}}$); therefore, the volume-weighted average values in each cross-section ($\emptyset_{ave} = \frac{1}{V_{total}} \sum_{i=1}^{i=n} \emptyset_i V_i$ where V is cell volume) were used rather than in one specific element.

8 Validation

8.1 Experimental setup

The full details of the validation experiments are provided in Meyer and Everts [2]. Forced convection conditions were obtained at a Reynolds number of 941 and heat flux of 60 W/m^2. The average fully developed Nusselt number ($50 < z/D < 827$) was within 8.9% of the theoretical value of 4.36 for fully developed forced convection laminar flows. The results also correlated well with the correlation of Shah and London [45] with an average deviation of 19%, while the deviation between $z/D = 567$ and $z/D = 724$ was less than 3%. The local mixed convection Nusselt numbers were compared with the fully developed flow correlation of Morcos and Bergles [38]. The results correlated well with an average deviation of 6% ($37 < z/D < 827$). Furthermore, the average mixed convection Nusselt numbers were within 2% of the correlation of Morcos and Bergles [38].

8.2 Numerical model

Figure 6 compares the local Nusselt numbers of the numerical results (solid green line) with the experimental data (red markers) at different Grashof numbers. The error bars indicate the uncertainties in the experimental data. This figure indicates that the results of the numerical simulations correlated well with the experimental data and similar trends were obtained. Furthermore, the average deviation between the experimental and numerical results was 4%, which was less than the average uncertainty of 4.3%. Therefore, there was good agreement between the numerical model and experimental results.

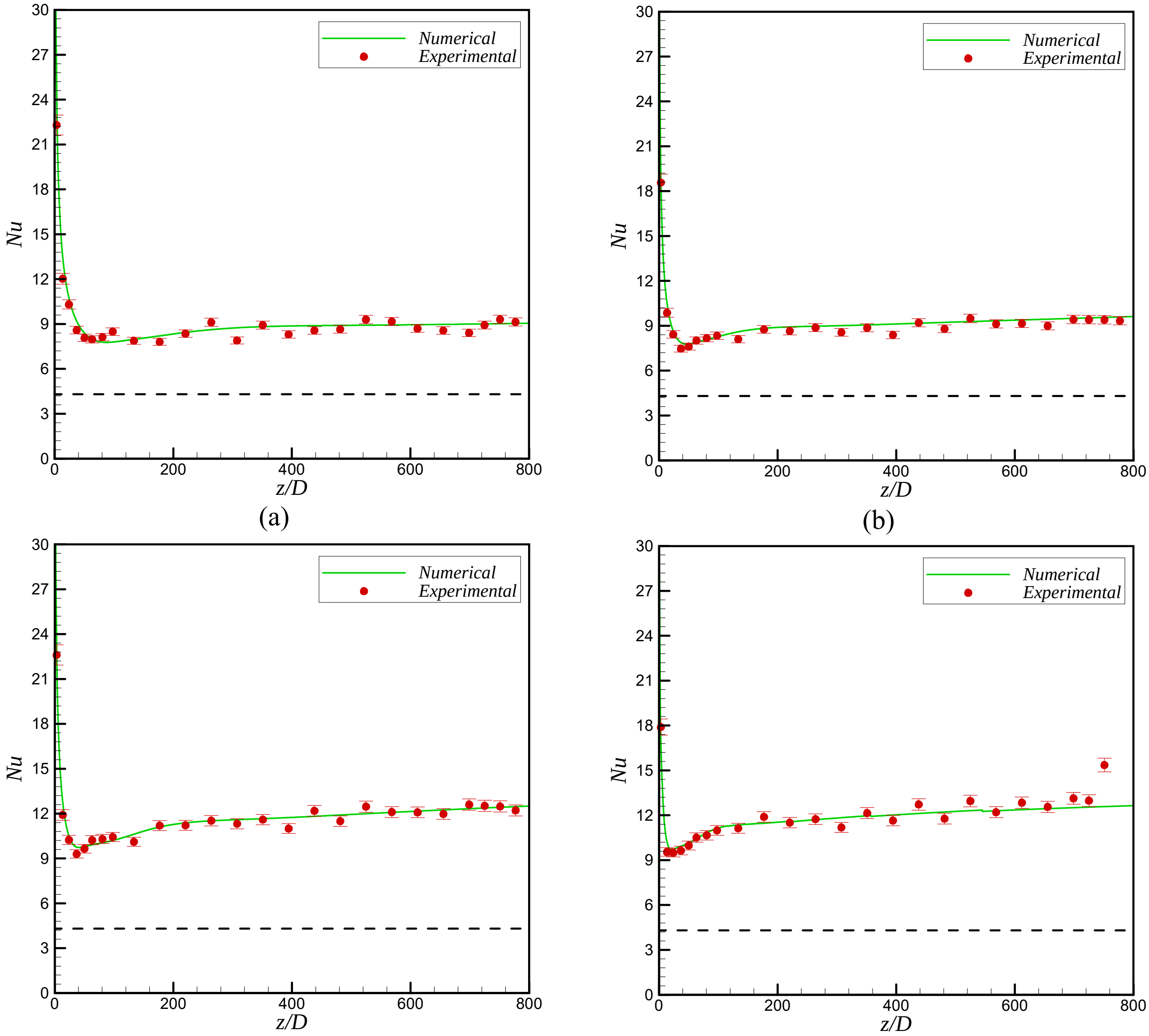

(a) (b) (c) (d)

Figure 6: Comparison of the experimental and numerical local Nusselt numbers as a function of axial position for Grashof numbers of (a) 8.7×10^3 (Re = 1 800 and $\dot{q}$ = 1 kW/m^2), (b) 1.0×10^4 (Re = 1 000 and $\dot{q}$ = 1 kW/m^2), (c) 3.4×10^4 (Re = 1 800 and $\dot{q}$ = 3 kW/m^2), and (d) 5.5×10^4 (Re = 1 000 and $\dot{q}$ = 3 kW/m^2).

For mixed convection conditions, significant temperature gradients existed in the cross-section of the tube caused by buoyancy effects. Therefore, the surface temperatures at the tube's top, bottom and side were compared, as shown in Figure 7. There was an excellent agreement between numerical and experimental results; and it was therefore concluded that the numerical model could accurately simulate the experimental conditions.

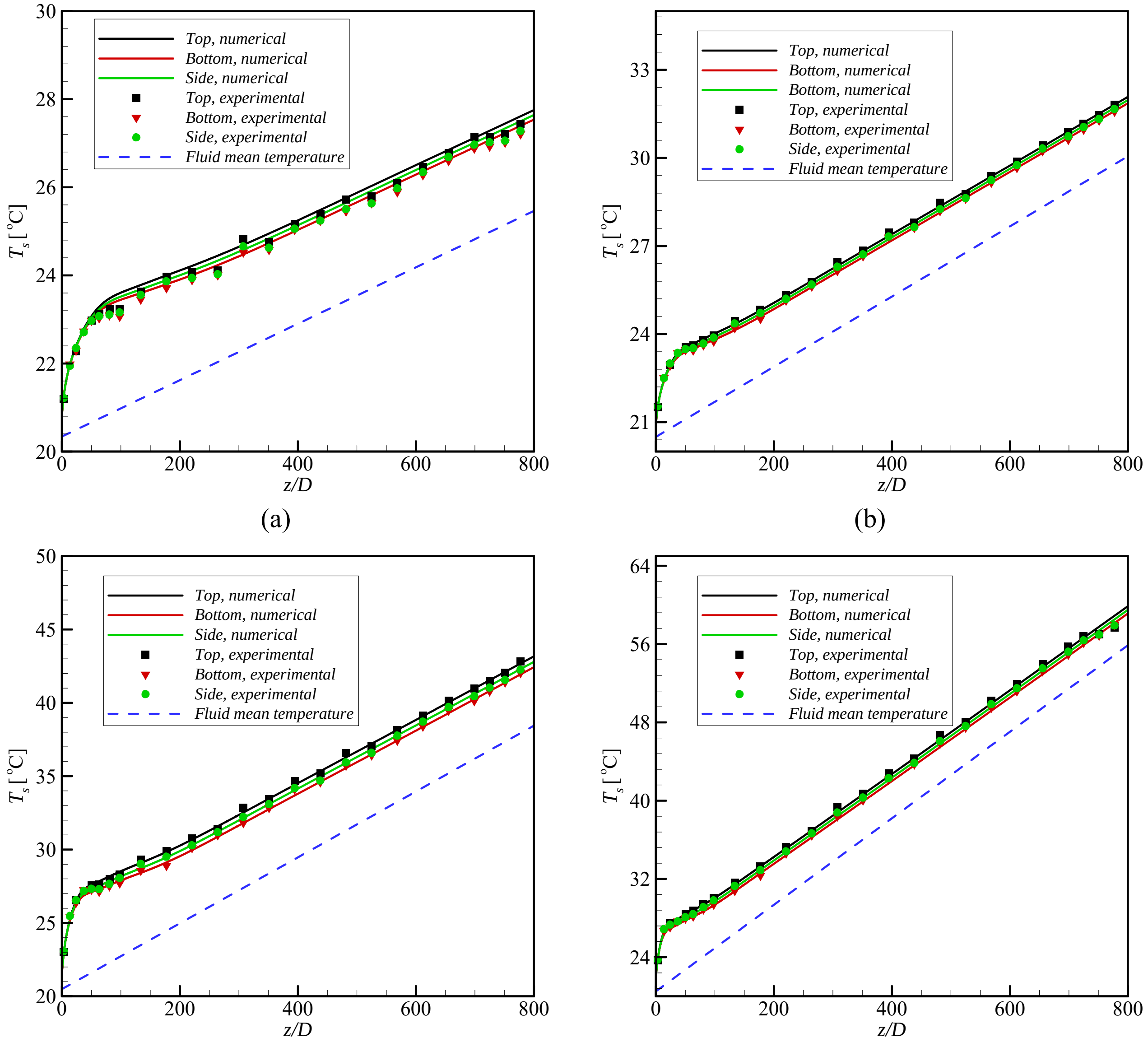

(a) (b)

(c) (d)

Figure 7: Surface temperature at the top, bottom and side locations of the tube for Grashof numbers of (a) 8.7×10^3 (Re = 1 800 and $\dot{q}$ = 1 kW/m^2), (b) 1.0×10^4 (Re = 1 000 and $\dot{q}$ = 1 kW/m^2), (c) 3.4×10^4 (Re = 1 800 and $\dot{q}$ = 3 kW/m^2), and (d) 5.5×10^4 (Re = 1 000 and $\dot{q}$ = 3 kW/m^2).

9 Results and discussion

9.1 Local Nusselt numbers

To investigate the effect of buoyancy on the development of the heat transfer coefficients, Figure 8 compares the local Nusselt numbers of five different Grashof numbers. Using the flow regime maps of Everts and Meyer [11], forced convection conditions were predicted for a Grashof number of 810, while the other four cases were identified as mixed convective flow. The different Grashof numbers were obtained by conducting experiments at different heat fluxes and Reynolds numbers.

Figure 8 indicates that for forced convection conditions (Gr = 810), the local Nusselt numbers decreased along the tube length and became approximately constant and equal to the theoretical Nusselt number of 4.36. At a fixed Reynolds number of 1 000, the black, green and red data indicate that the magnitude of the Nusselt numbers increased significantly when the heat flux (and thus

Grashof number) increased. This was due to the buoyancy effects that enhanced heat transfer inside the tube. Furthermore, the local mixed convective Nusselt numbers did not decrease and become constant, but formed a trough and increased slightly before becoming constant and fully developed. This led to three distinct laminar regions, which were defined as forced convection developing, mixed convection developing and fully developed by Meyer and Everts [2]. The green and red data also indicate that the gradient of the increasing local Nusselt numbers in the mixed convection developing region increased with increasing Grashof number.

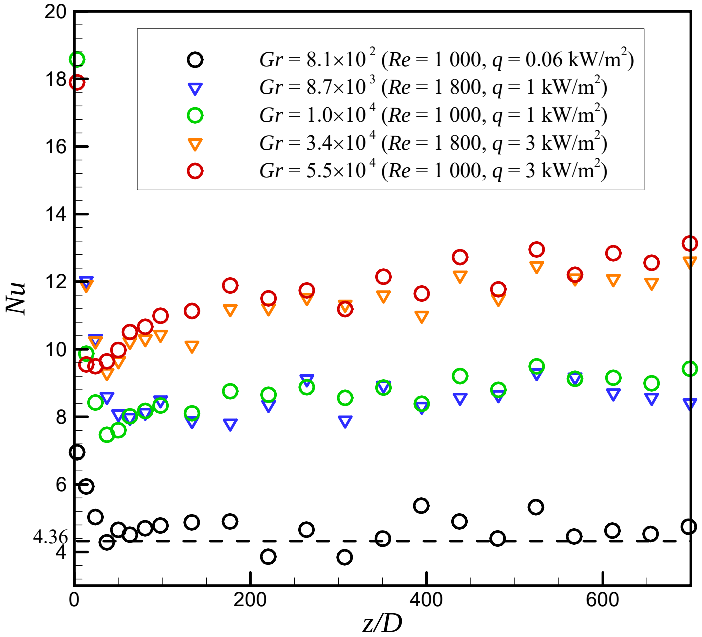

Figure 8: Comparison of Nusselt numbers as a function of axial position for different Grashof numbers. The black markers represent the forced convection results, while the blue, green, orange and red markers represent the mixed convection results.

Meyer and Everts [2] postulated that the three distinct laminar regions occurred due to the development of the thermal boundary layer and the influence of buoyancy effects. The hydrodynamic and thermal boundary layers (Section 9.2), temperature (Section 9.3) and velocity profiles (Section 9.4), secondary flow strength (Section 9.5), as well as the forces that were present in the boundary layers (Section 9.6) were therefore investigated in this paper to gain a thorough understanding of the factors that caused the changes in the mixed convective flow trends compared to forced convective flow.

9.2 Hydrodynamic and thermal boundary layers

To obtain the hydrodynamic boundary layer, Figure 9 contains the absolute value of *y*-velocity gradient at different axial positions for a Reynolds number of 1 000 and a heat flux of 3 kW/m^2. The hydrodynamic boundary layer's edge is considered the location (in the *y*-direction) where the velocity gradient first reached a minimum value (in both the upper and lower part of the tube). Figure 9 indicates that at *z*/*D* = 1.7, the hydrodynamic boundary layer thickness was approximately 2.56 mm in both the upper and lower part of the tube. It then increased along the tube length and merged at *z*/*D* = 7. At *z*/*D* = 11, the hydrodynamic boundary layer thickness in the upper part of the tube was slightly greater than in the lower part of the tube. The merging point of the boundary layers continued to shift downwards and at *z*/*D* = 95, the boundary layer thickness was approximately 1.8 times greater in the upper part of the tube than in the lower part. This was due to the presence of secondary flow inside the tube, which is further investigated in Sections 9.3 and 9.4.

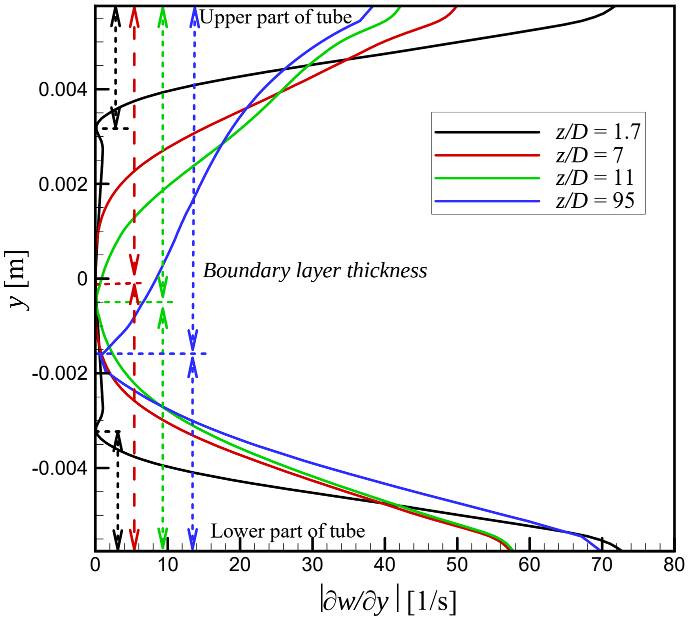

Figure 9: *Y*-velocity gradient along the tube length for a Reynolds number of 1 000 and heat flux of 3 kW/m^2 to obtain the hydrodynamic boundary layer. The first location with a zero-velocity gradient corresponds to the hydrodynamic boundary layer thickness.

Because vorticity is associated with the rotation of a fluid element due to the induced velocity gradient in all directions, it can also provide information regarding the exact location of the merging boundary layer. Therefore, complementary to the velocity gradients in Figure 9, Figure 10 compares the vorticity magnitude at different cross-sectional positions along the tube length for a Reynolds number of 1 000 and heat flux of 3 kW/m^2. This figure confirms that the hydrodynamic boundary layers merged at *z/D* = 7, because it corresponded to the minimum vorticity magnitude along the tube centre line. The initial gradual change in vorticity is related to the mass flow change in the inviscid region due to the formation of the boundary layer from the wall. A significant change in vorticity occurs when the boundary layer merges and a sharp drop to zero followed by an increase in vorticity was obtained.

To obtain the thermal boundary layer, Figure 11 contains the temperature gradient in the *y*-direction at different axial positions for a Reynolds number of 1 000 and heat flux of 3 kW/m^2. Similar to Figure 9, the edge of the thermal boundary layer corresponded to the location (in the *y*-direction) where the temperature gradient first reached a minimum value (in the upper and lower part of the tube).

Figure 11 indicates that at *z/D* = 7, the thermal boundary layer thickness was approximately 2.56 mm and 2.16 mm in both the upper and lower part of the tube, respectively. The boundary layer thickness in the upper part of the tube increased significantly along the tube length, while the changes in the lower part of the tube were minimal. At *z/D* = 40, the boundary layers merged far below the centre line of the tube at *y* = -0.0033 m. The merging point of the boundary layers continued to shift downwards and at *z/D* = 60, the boundary layer thickness in the upper part of the tube was approximately 4.7 times greater than in the lower part of the tube. Similar to the hydrodynamic boundary layer, this was due to the presence of secondary flow inside the tube, which is further discussed in Sections 9.3 and 9.4.

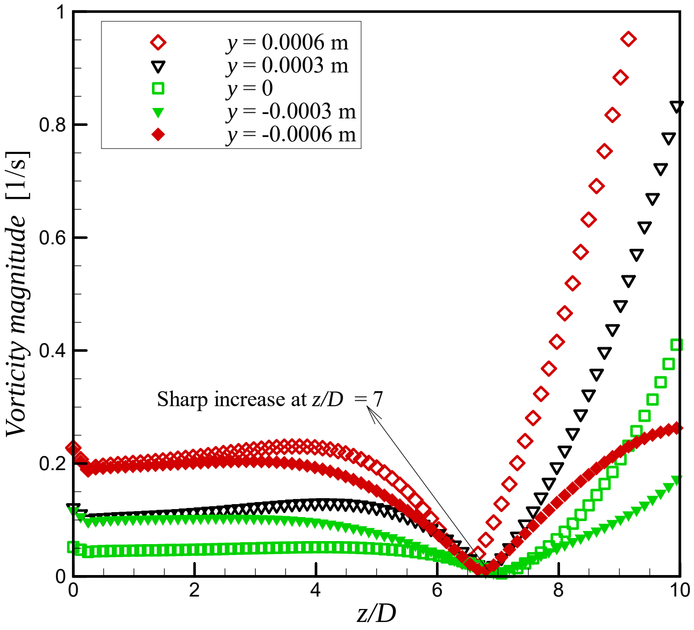

Figure 10: Vorticity magnitude at different cross-sectional positions along the tube length for a Reynolds number of 1 000 and heat flux of 3 kW/m^2 to obtain the axial position of the merged hydrodynamic boundary layers.

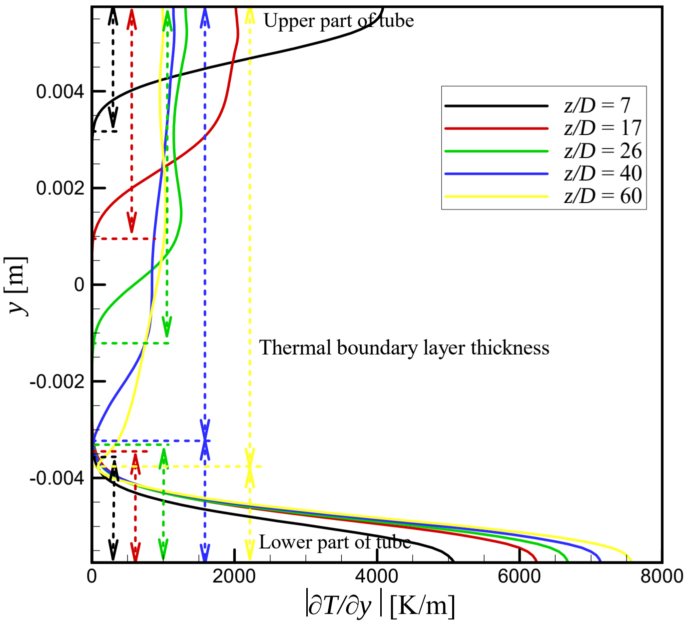

Figure 11: Temperature gradient in the *y*-direction along the tube length for a Reynolds number of 1 000 and heat flux of 3 kW/m^2 to obtain the thermal boundary layer. The first location with zero temperature gradient corresponds to boundary layer thickness.

To investigate the development of the hydrodynamic and thermal boundary layers for mixed convective flow, Figure 12 compares hydrodynamic and thermal boundary layers on the vertical symmetrical plane along the tube length for different Grashof numbers. The hydrodynamic boundary layer merged near the centre line of the tube shortly after the inlet for all Grashof numbers. Furthermore, the axial position at which the hydrodynamic boundary layer merged, decreased with decreasing Reynolds number (Figure 12(a) and (b)), as well as with increasing heat flux and thus Grashof number (Figure 12(b) and (d)). As expected, the influence of Reynolds number was greater than the influence of Grashof number, because buoyancy-induced secondary flow was not yet significant near the tube inlet [2].

Unlike for forced convection conditions, the merging position did not remain near the centre line of the tube. Instead, it formed a trough and a peak before it became approximately constant along the tube length. When comparing the development of both the hydrodynamic and thermal boundary layers inside the tube, it follows that the trough in the hydrodynamic boundary layer corresponded to the axial position at which the thermal boundary layer merged. Furthermore, the peak in the hydrodynamic boundary layer corresponded to the axial position at which the thermal boundary layer thickness became constant along the tube length. Similar to the axial position at which the boundary layer merged, the axial positions of the hydrodynamic boundary layer trough and peak decreased with decreasing Reynolds number (Figure 12(a) and (b)), as well as with increasing heat flux and thus Grashof number (Figure 12(b) and (d)).

These trends suggested the hydrodynamic entrance length would decrease with decreasing Reynolds number and increasing Grashof number. However, an interesting observation from Figure 12 was that the axial position at which the hydrodynamic boundary layer thickness became constant, increased with increasing Grashof number. This was in good agreement with the findings of Everts and Meyer [12] namely that an increasing Grashof number (and thus buoyancy effects) disturbed the development of the hydrodynamic boundary layer, thus leading to an increased hydrodynamic entrance length compared with that of forced convective flow.

Figure 12 indicates that the thermal boundary layer growth was suppressed in the lower part of the tube when the hydrodynamic boundary layer merged, while the thermal boundary layer thickness continued to increase rapidly along the tube length in the upper part. After the thermal boundary layer merged significantly below the centre line of the tube, the merging position continued to shift downwards along the tube length to an asymptotic position. The thermal boundary layer thickness became constant along the tube length once the flow became thermally fully developed. The axial position at which the thermal boundary layer merged, decreased with decreasing Reynolds number (Figure 12(a) and (b)), as well as with increasing heat flux and thus Grashof number (Figure 12(b) and (d)). Furthermore, Figure 12 indicates that the axial position at which the thermal boundary layer thickness became constant decreased with increasing Grashof number. Therefore, similar to the findings of Everts and Meyer [12], increased buoyancy effects assisted the thermal boundary layers in developing, thus leading to a decreased thermal entrance length compared with that of forced convective flow.

To gain a visual understanding of the mutual influence of the development of the hydrodynamic and thermal boundary layers during mixed convective flow, Figure 13 shows the three-dimensional thermal boundary layer (dark blue region), the radial temperature gradient contours, as well as the tracked fluid elements along the tube (red arrows) for different Grashof numbers. The lines and arrows represent each computational cell's velocity tangent to the tracked element.

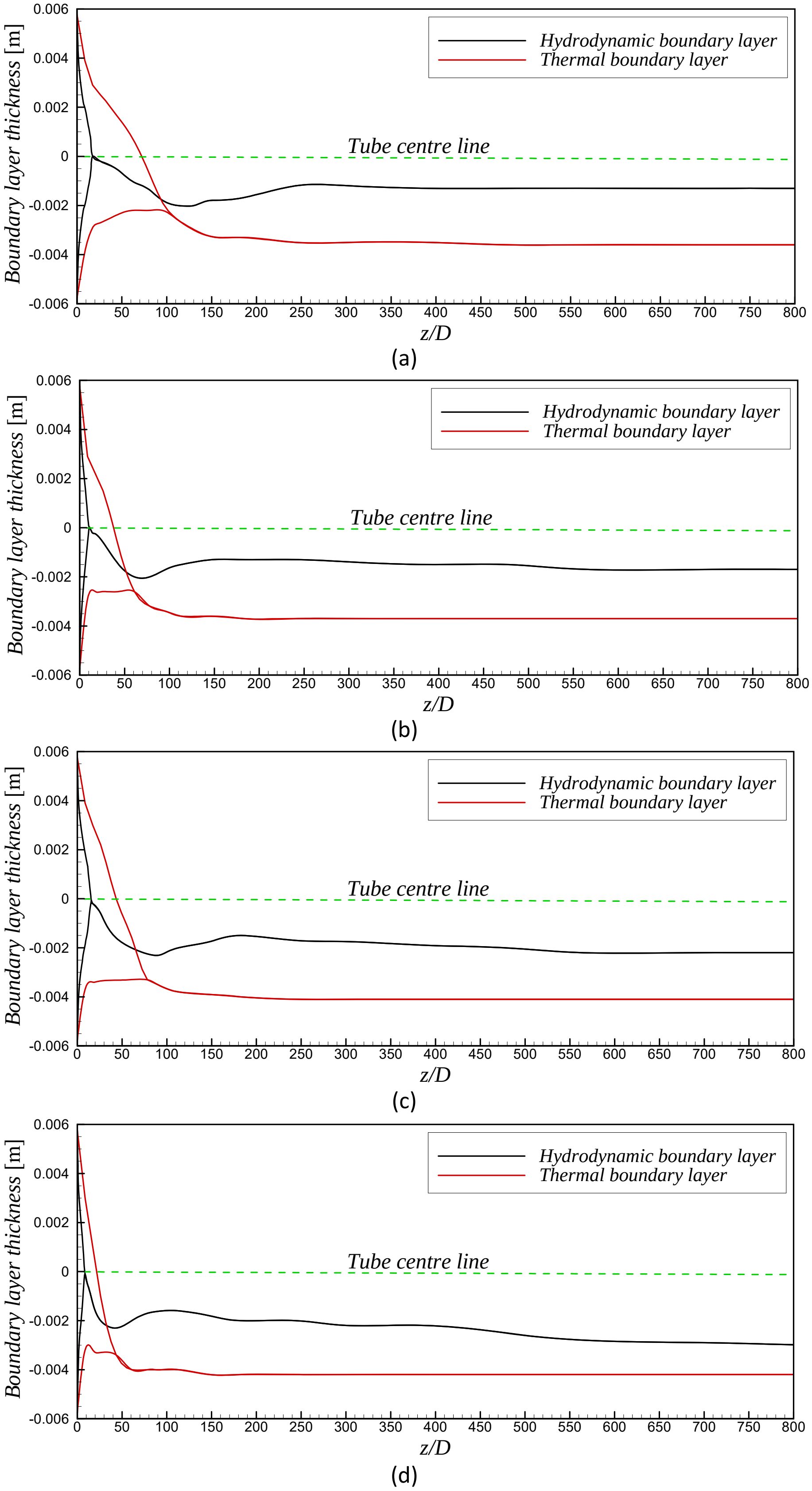

Figure 12: Development of the hydrodynamic and thermal boundary layers for Grashof numbers of (a) 8.7×10^3 (*Re* = 1 800 and $\dot{q}$ = 1 kW/m^2), (b) 1.0×10^4 (*Re* = 1 000 and $\dot{q}$ = 1 kW/m^2), (c) 3.4×10^4 (*Re* = 1 800 and $\dot{q}$ = 3 kW/m^2), and (d) 5.5×10^4 (*Re* = 1 000 and $\dot{q}$ = 3 kW/m^2).

In general, the thermal boundary layer developed rapidly near the inlet of the tube, but the boundary layer growth decreased when approaching the merging point. Figure 13(b) indicates that the flow was parallel near the inlet of the tube, but developed a ‘wavy’ nature from approximately z = 0.7 m when the thermal boundary layer merged (at z/D = 60 from Figure 12(b)). The ‘wavy’ nature was due to significant secondary flow inside the tube. This nature initially started due to buoyancy effects, which could be compared with momentum in the flow cross-section, and then stabilised at approximately z = 1.3 m when the thermal boundary layer thickness became constant (at z/D = 115 from Figure 12(b)). Furthermore, it contributed to the upward movement of the hydrodynamic boundary layer merging point in Figure 12 once the thermal boundary layers merged. Figure 13 also indicates that as the Grashof number, and thus mixed convection, increased, the ‘wavy’ nature in the fluid layers increased and started earlier along the tube length with increasing Grashof number. These cross-sectional circulations could therefore be justified with x- and y-vectors of velocity using streamlines (Section 9.3).

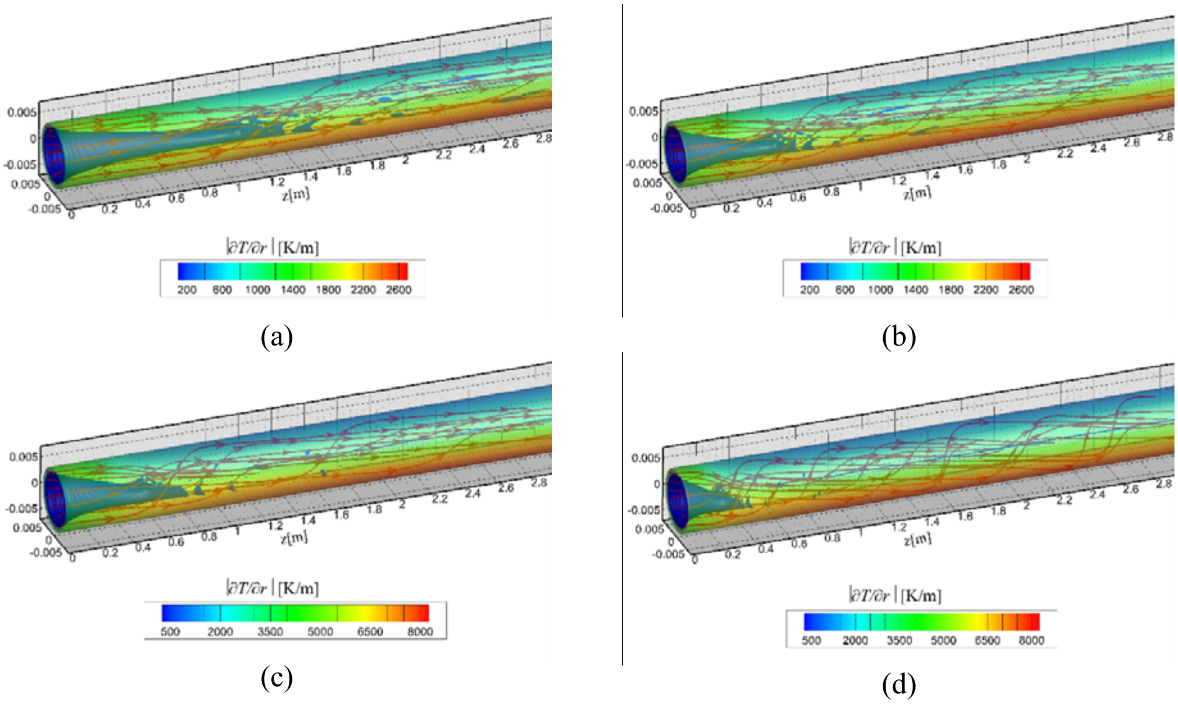

(a) (b)

(c) (d)

Figure 13: Three-dimensional presentation of the development of the thermal boundary layer (dark blue region) in the tube for Grashof numbers of (a) 8.7×10^3 (Re = 1 800 and $\dot{q}$ = 1 kW/m^2), (b) 1.0×10^4 (Re = 1 000 and $\dot{q}$ = 1 kW/m^2), (c) 3.4×10^4 (Re = 1 800 and $\dot{q}$ = 3 kW/m^2), and (d) 5.5×10^4 (Re = 1 000 and $\dot{q}$ = 3 kW/m^2). The red lines represent the streamlines tangent to the velocity vector.

9.3 Temperature profiles

Figure 14 contains the temperature contours and the secondary flow streamlines at different cross-sections for a Reynolds number of 1 000 and heat flux of 1 kW/m^2. The purple and red markers represent the merging positions of the hydrodynamic and thermal boundary layers (Figure 12), respectively. As the tube was heated at a constant heat flux, the fluid temperature increased linearly along the tube length. Figure 14 indicates that a temperature gradient existed at each cross-section. The fluid near the tube surface had a higher temperature (and lower density), while the fluid in the tube centre had a lower temperature (and higher density). In the presence of gravity, the low-density fluid circulated upwards near the tube surface. The high-density fluid circulated downwards in the tube centre to conserve continuity in the cross-section. This led to the formation of two symmetrical vortices, as indicated by the streamlines in Figure 14 [1, 16, 31].

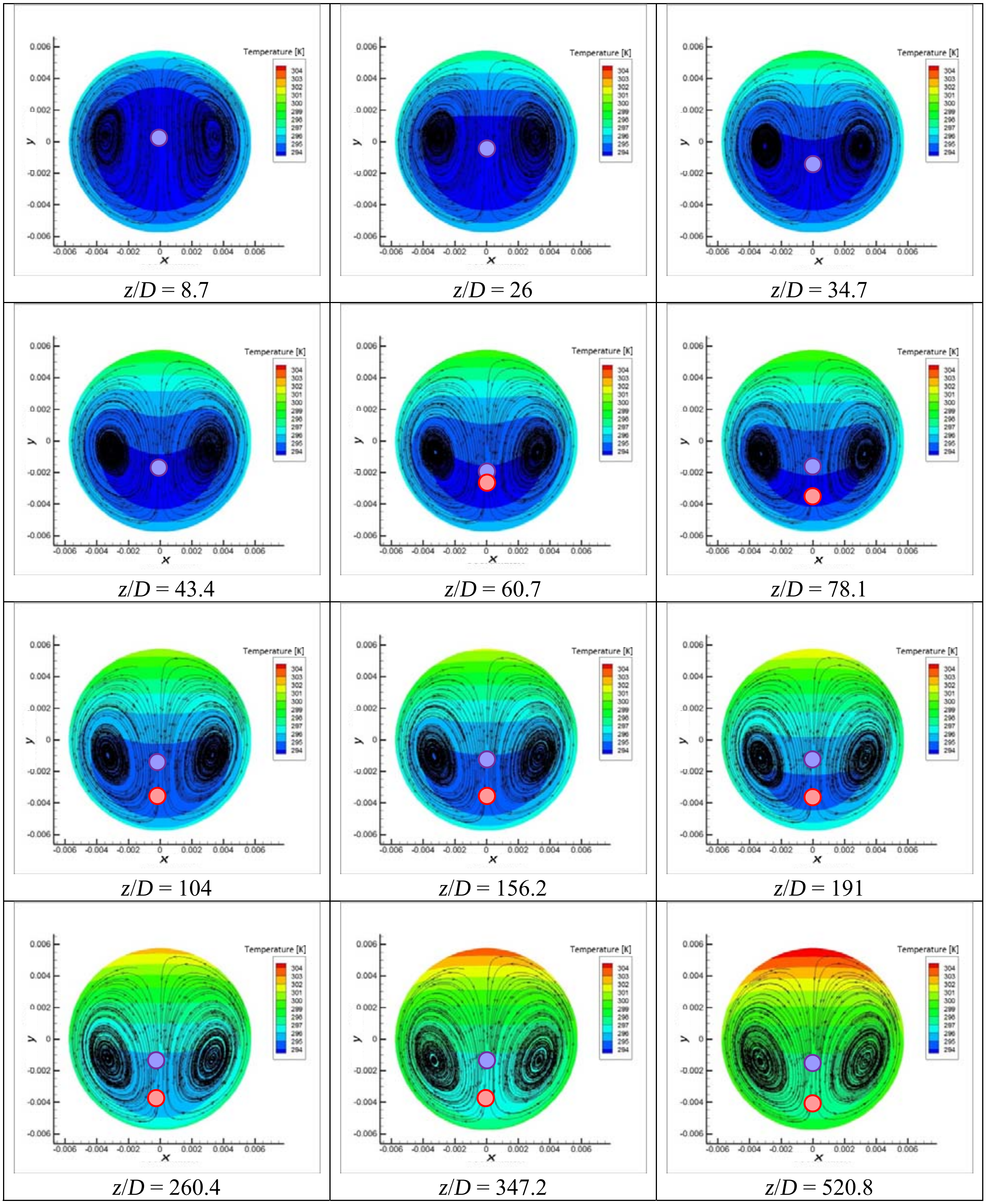

z/*D* = 8.7

z/*D* = 26

z/*D* = 34.7

z/*D* = 43.4

z/*D* = 60.7

z/*D* = 78.1

z/*D* = 104

z/*D* = 156.2

z/*D* = 191

z/*D* = 260.4

z/*D* = 347.2

z/*D* = 520.8

Figure 14: Temperature contours (in Kelvin) and secondary flow streamlines at different axial positions along the tube length for a Reynolds number of 1 000 and heat flux of 1 kW/m^2. The purple and red markers represent the merging positions of the hydrodynamic and thermal boundary layers (Figure 12(b)) respectively.

These two vortices assisted in distributing the heat from the surface to the centre of the tube. Due to the presence of buoyancy, a high-temperature region formed near the top of the tube. Furthermore, the streamlines indicate that this high-temperature region was less active than the bottom of the tube, which explains why the thermal boundary layer thickness was greater in the upper than the lower part of the tube, as shown in Figure 12. The two vortices moved downwards and sideways (toward the tube surface) along the tube length. An interesting observation from Figure 14 was that the centre of the vortices was always above the merging position of the hydrodynamic (purple markers) and thermal (red markers) boundary layers and closer to the merging position of the hydrodynamic boundary layer. Furthermore, the minimum cross-sectional temperature region corresponded well to the merging position of the thermal boundary layer, because the merging position of the thermal boundary layer occurred closer to the bottom of the tube, below the centre of the vortices.

9.4 Velocity profiles

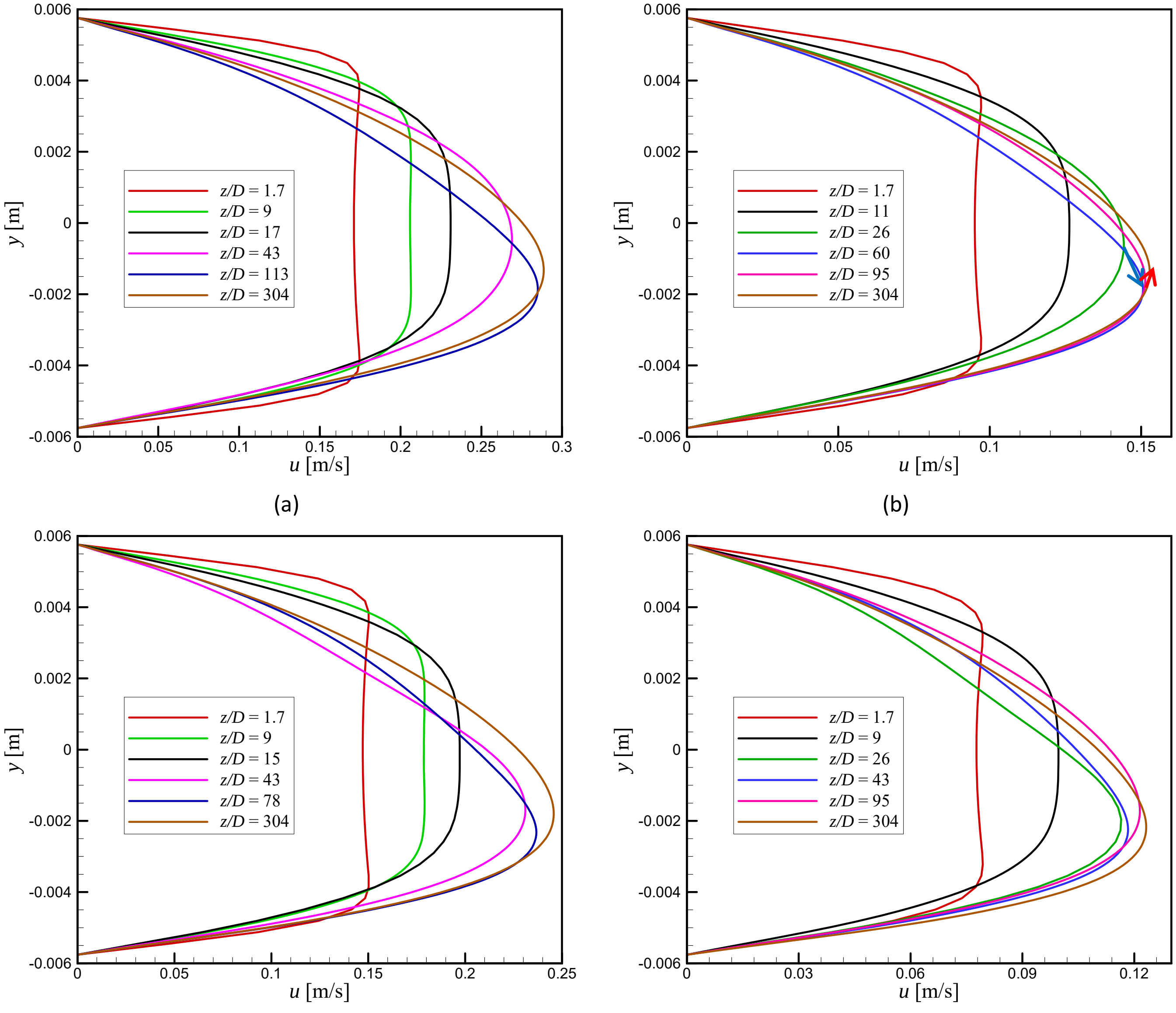

(a) (b)

(c) (d)

Figure 15: Cross-sectional velocity profiles along the tube length for Grashof numbers of (a) 8.7×10^3 ($Re = 1\,800$ and $\dot{q} = 1$ kW/m^2), (b) 1.0×10^4 ($Re = 1\,000$ and $\dot{q} = 1$ kW/m^2), (c) 3.4×10^4 ($Re = 1\,800$ and $\dot{q} = 3$ kW/m^2), and (d) 5.5×10^4 ($Re = 1\,000$ and $\dot{q} = 3$ kW/m^2). The blue and red arrows in (b) indicates that the peak of the velocity profile reached a minimum at approximately $z/D = 60$ and the moved slightly upwards further along the tube length.

Figure 15 compares the cross-sectional velocity profiles along the tube length for different Grashof numbers. The velocity profiles are shown in Figure 15(b), corresponded to the temperature profiles in Figure 14. Figure 15(b) indicates that the velocity profile was symmetric near the tube inlet. This was as expected, as Meyer and Everts [2] found that buoyancy effects were suppressed near the tube inlet. After the hydrodynamic boundary layer merged, the velocity profile became asymmetric, which is in good agreement with the hydrodynamic boundary layers, shown in Figure 12(b). The degree of asymmetry increased with increasing buoyancy effects along the tube length. The blue arrow indicates that the peak of the velocity profile reached a minimum at approximately $z/D = 60$, which corresponded to the trough in the hydrodynamic boundary layer, shown in Figure 12(b), and also to the axial position at which the thermal boundary layer merged.

Figure 12(b) indicates that after the hydrodynamic boundary layer merging position reached a minimum, it moved slightly upwards along the tube length. This trend is confirmed by the red arrow in Figure 15(b). The peak of the velocity profile moved downwards as the high-temperature (and less active) region in the upper half of the tube increased along the tube length (Figure 14). However, as the cross-sectional temperature differences increased along the tube length, the buoyancy force developed and became sufficient to move the velocity profile peak and hydrodynamic boundary layer merging position upwards. When comparing the velocity profiles at different Grashof numbers in Figure 15, it follows that increasing Grashof numbers led to an asymmetric velocity profile earlier along the tube and the axial position at which the peak of the velocity profile reached a minimum occurred earlier.

To better understand the influence of buoyancy on the velocity profile, Figure 16 contains the velocity contours and secondary flow streamlines, at different cross-sections, for a Reynolds number of 1 000 and heat flux of 1 kW/m^2. The purple and red markers represent the merging positions of the hydrodynamic and thermal boundary layers (Figure 12), respectively. As expected, the velocity increased from approximately zero near the tube wall (blue regions) to a maximum in the centre of the tube (red region).

The velocity profile was symmetric and uniform near the tube's inlet (at $z/D = 8.7$), with the centres of the two vortices slightly above the centre line and the peak of the velocity profile (red region) slightly below the centre line. At $z/D = 26$, after the hydrodynamic boundary layers merged, the vortices had a slight downward shift, while the peak of the velocity profile experienced a significant downward shift, and the velocity profile was no longer symmetric. As the velocity profile developed along the tube length and the fluid temperature increased, buoyancy effects increased, leading to a greater stagnant high-temperature region near the top of the tube (Figure 14). This caused the velocity profile peak and vortices to move downwards between $z/D = 26$ and $z/D = 60.7$. After the velocity profile peak reached a minimum at approximately $z/D = 60$ (Figure 12(b)), the two vortices continued to move downwards, but the velocity profile peak moved upwards.

Figure 16 also indicates that the shape of the maximum velocity region was approximately circular near the tube's inlet, but changed to an egg shape along the tube length as buoyancy increased. After the merging position of the hydrodynamic boundary layer reached a maximum at approximately $z/D = 160$ in Figure 12(b), the peak and shape of the velocity profile remained approximately constant along the tube length, while the centres of the two vortices continued to experience a slight downward shift ($z/D > 156.2$ in Figure 16) as the flow approached hydrodynamically fully developed flow. The temperature (Figure 14) and velocity (Figure 16) contours indicate that the secondary flow vortices played an important role in the flow field and thermal features of mixed convective flow.

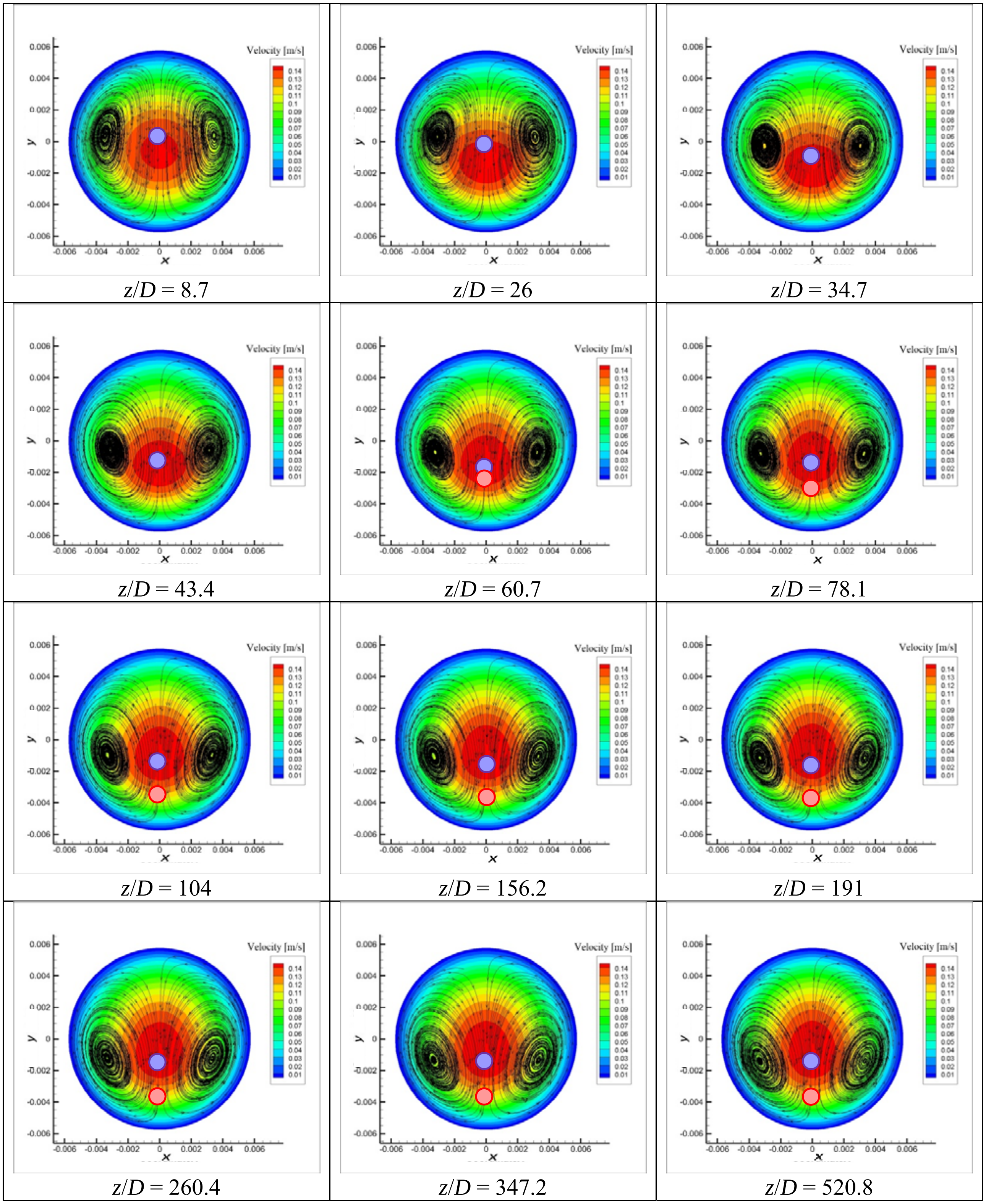

z/D = 8.7 z/D = 26 z/D = 34.7

z/D = 43.4 z/D = 60.7 z/D = 78.1

z/D = 104 z/D = 156.2 z/D = 191

z/D = 260.4 z/D = 347.2 z/D = 520.8

Figure 16: Velocity contours and secondary flow streamlines at different axial positions along the tube for a Reynolds number of 1 000 and heat flux of 1 kW/m^2. The purple and red markers represent the merging positions of the hydrodynamic and thermal boundary layers (Figure 12(b)), respectively.

Figure 17 compares the development of the cross-sectional velocity profiles along the tube length for Reynolds numbers of 1 000 and 1 800 at a heat flux of 1 kW/m^2. This figure illustrates how the initial circular velocity profile started changing to an egg shape after a certain distance from the inlet. Figure

17(b) indicates that when the Reynolds number was increased to 1 800, a longer tube length was required before the velocity profile started changing. Furthermore, the egg shape profile was less pronounced than at a Reynolds number of 1 000 (Figure 17(a)). This was expected because buoyancy effects decreased with increasing Reynolds number due to the decreased cross-sectional temperature differences, and therefore, the impact on the velocity profile was less.

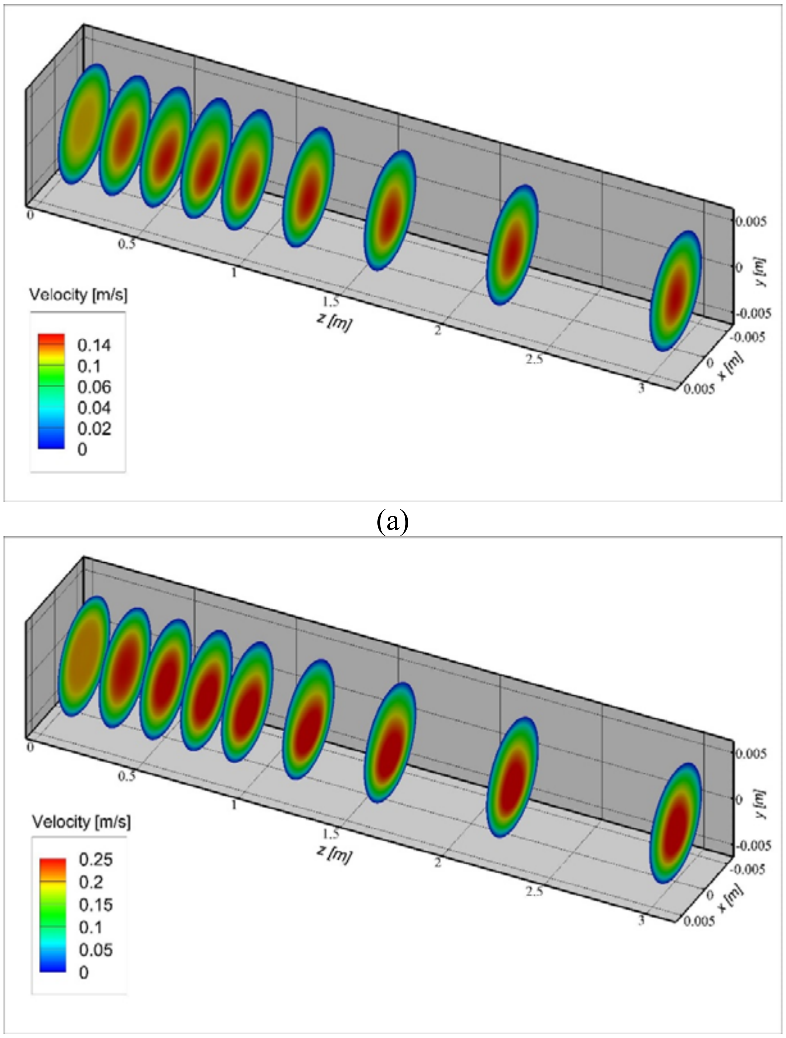

(a)

(b)

Figure 17: Development of the velocity profile along the tube length for Reynolds numbers of (a) 1 000 and (b) 1 800 and a heat flux of 1 kW/m^2.

9.5 Secondary flow strength

To quantitatively investigate the effects of secondary flow, a new parameter namely the secondary flow strength (SFS), was defined. In its simplest definition, the secondary flow strength consists of the ratio of the cross-sectional velocity to the overall velocity:

$$SFS = \frac{\sqrt{u^2 + v^2}}{\sqrt{u^2 + v^2 + w^2}} \tag{29}$$

Therefore, the secondary flow strength represents the additional cross-sectional flow circulations. The average secondary flow strength in each cross-section (720 computational cells) was calculated along the tube length. Figure 18 compares the local Nusselt numbers (solid black lines) and secondary flow strength (solid red lines) for different Grashof numbers. Furthermore, the simulations were also repeated without buoyancy (dotted blue lines) to clarify the effect of secondary flow on the local Nusselt number trends.

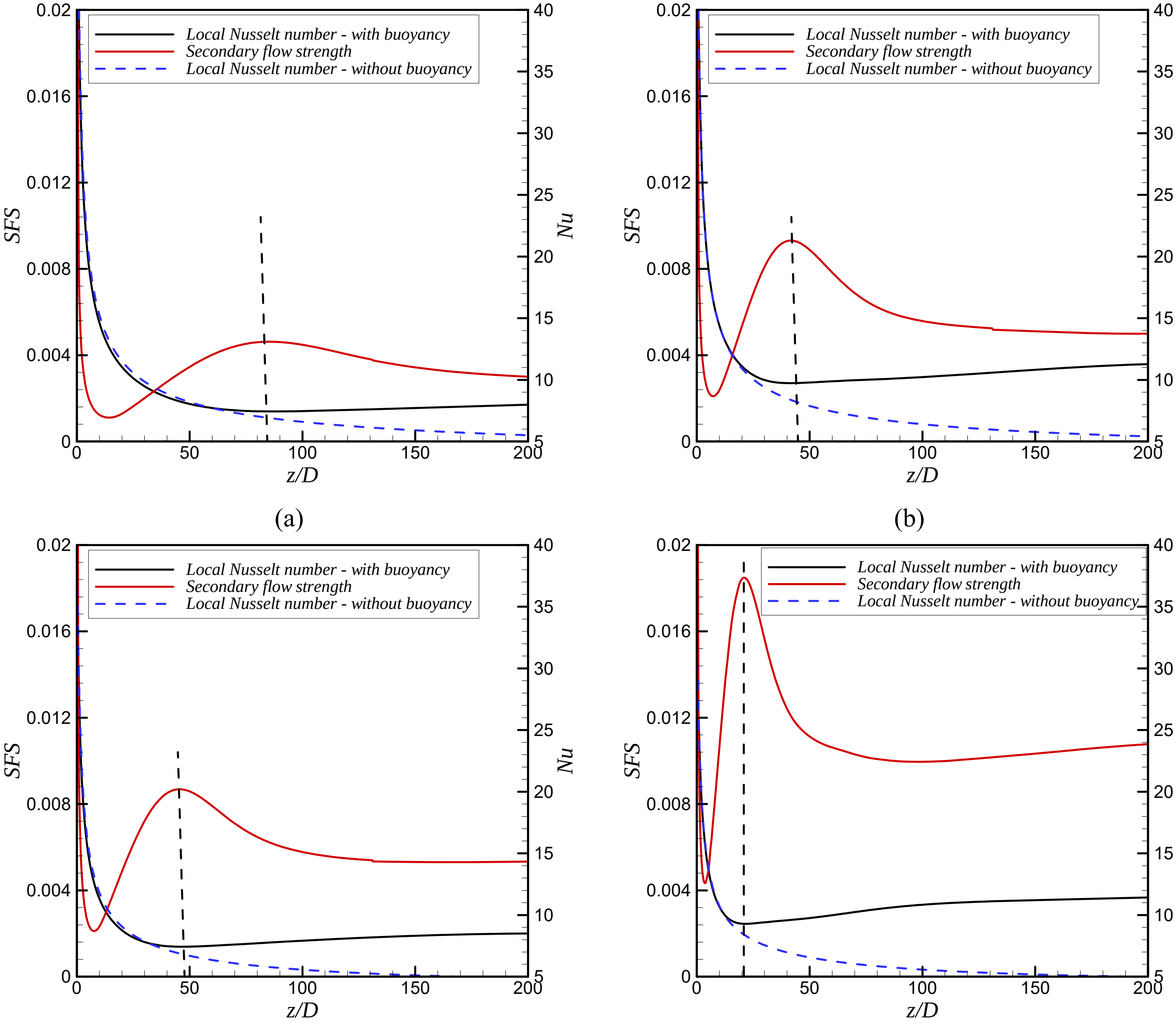

(a)

(b)

(c)

(d)

Figure 18: Comparison of secondary flow strength (dotted black lines) and local Nusselt numbers (solid red lines) as a function of axial position for Grashof numbers of (a) 8.7×10^3 (*Re* = 1 800 and $\dot{q}$ = 1 kW/m^2), (b) 1.0×10^4 (*Re* = 1 000 and $\dot{q}$ = 1 kW/m^2), (c) 3.4×10^4 (*Re* = 1 800 and $\dot{q}$ = 3 kW/m^2), and (d) 5.5×10^4 (*Re* = 1 000 and $\dot{q}$ = 3 kW/m^2).

The maximum secondary flow strength was found at the inlet of the tube, which then rapidly decreased to a minimum, increased again to form a peak before it decreased. This trend was due to the presence of two different types of secondary flow inside the tube: (1) shear stress-driven secondary flow (Figure 19(a)) and (2) buoyancy-driven secondary flow (Figure 19(b)). When the hydrodynamic boundary layer started forming from the tube inlet, the streamlines in Figure 19(a) indicate radial flow towards the centre of the tube due to continuity conservation, which led to shear stress-driven secondary flow. As the hydrodynamic boundary layer thickness increased along the tube length, less radial flow occurred, causing the shear stress-driven secondary flow and secondary flow strength to decrease from the tube inlet in Figure 18. The negligible difference between the solid black and dotted blue lines confirm that buoyancy-driven secondary flow was not yet significant.

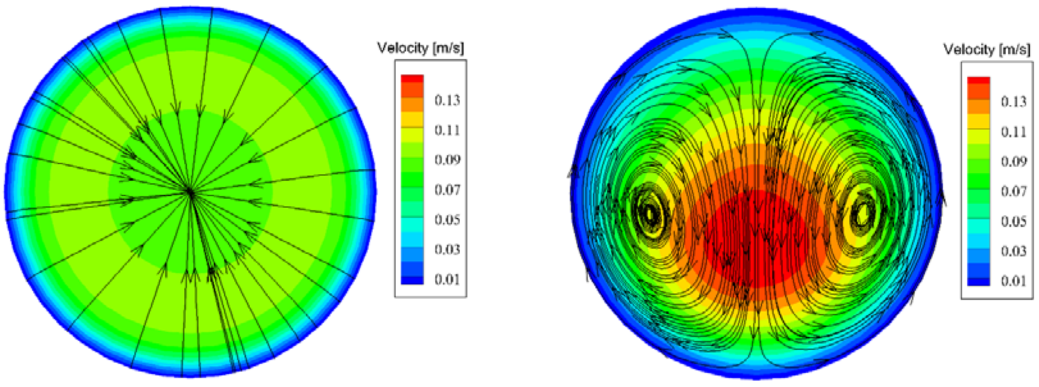

(a) (b)

Figure 19: Two types of secondary flow: (a) shear stress-driven secondary flow due to the boundary layer formation near the inlet (z/D = 1.0) and (b) buoyancy-driven secondary flow at z/D = 95.4.

Because the tube was heated at a constant heat flux, cross-sectional temperature differences existed, which led to the formation of thermal boundary layers from the tube inlet. Due to these cross-sectional temperature differences (and thus density differences), buoyancy effects led to the formation of two symmetrical vortices (Figure 14 and Figure 16). As the thermal boundary layer thickness and surface-fluid temperature differences increased along the tube length, the buoyancy-driven secondary flow (Figure 19(b)) increased. Once the increasing buoyancy-driven secondary flow began to dominate the decreasing shear stress-driven secondary flow, the secondary flow strength began to increase along the tube length.

Between the trough and the peak of the red secondary flow strength curve, the buoyancy-induced secondary flow increased. The local Nusselt numbers (solid black line) began to deviate from the local Nusselt numbers without any buoyancy effects (dotted blue line), but the buoyancy-induced secondary flow was not yet sufficient to increase the heat transfer coefficients. The vertical black dotted lines in Figure 18 indicate that the peak of the secondary flow strength (red curve) corresponded to the trough in the Nusselt numbers (black curve). After the peak, the buoyancy force had to reach a balance with the cross-sectional momentum to eventually stabilise as the thermal boundary layer thickness became constant, which caused the secondary flow strength to decrease. However, the enhanced heat transfer due to the presence of the two secondary flow vortices was sufficient to increase the local Nusselt numbers. Furthermore, Figure 18(b) indicates that once the thermal boundary layer thickness became approximately constant (z/D = 160 in Figure 12(b)), the secondary flow strength and local Nusselt numbers became approximately constant as well.

Figure 18 also indicates that the magnitude of the secondary flow strength increased with increasing Grashof number, and the dotted black lines indicate that the peak in the secondary flow strength and trough in the local Nusselt numbers occurred earlier. This was in good agreement with the findings of Meyer and Everts [2], namely that the forced convection developing region decreased with increasing Grashof number.

9.6 Forces in boundary layer

Figure 20 compares the viscous, inertia, and combined buoyancy and pressure gradient forces along the tube length for different Grashof numbers. The trend of each force can be explained in terms of the nature and role of the specific force in the flow. The inertia force, which is the driving force for fluid flow, played a prominent role in the *y*-direction when the gradient of the *v* velocity, induced by the boundary layer formation, was introduced. The inertia force (proportional to the velocity gradient) was expected to be zero for the fully developed flow because the flow was no longer accelerating. Figure 20(b) indicates a significant change in the inertia force near the tube inlet as the hydrodynamic boundary layer developed. After the hydrodynamic boundary layer merged at $z/D = 7$ (Figure 12(b)), the magnitude of the inertia force began to decrease and, in the absence of buoyancy effects, would have approached zero for fully developed flow. However, due to the presence of secondary flow, the increasing secondary flow strength along the tube length (Figure 18(b)) caused the inertia force to increase. After the thermal boundary layers merged at $z/D = 60$ (Figure 12(b)), both the inertia force and the secondary flow strength decreased. Although the flow only became hydrodynamically fully developed at approximately $z/D = 550$ (Figure 12(b)), the changes in the velocity gradient became very small when the flow approached thermally fully developed flow, and the inertia force became zero and constant at approximately at $z/D = 110$ in Figure 20(b).

The viscous force, which is the shear stress gradient, increased as the hydrodynamic boundary layer developed from the tube inlet. The reason was that the fluid came into contact with the tube surface and began to influence the inviscid region as the fluid flow through the tube. Furthermore, the presence of secondary flow, which increased as the thermal boundary layer thickness increased, contributed to an increasing viscous force for $z/D < 45$ (Figure 12(b) and Figure 18(b)). The viscous force reached a maximum at $z/D = 45$, which also corresponded to the maximum secondary flow strength shown in Figure 18(b), and the minimum local Nusselt number. As the secondary flow strength began to decrease, the viscous force decreased to an asymptotic value. The axial position at which the viscous force became constant corresponds to the axial position at which the flow became thermally fully developed (hydrodynamic boundary layer merging point reached a maximum, and the thermal boundary layer thickness became constant in (Figure 12(b)).

The combined buoyancy and pressure gradient force trend was similar to that of the other forces; however, the changes along the tube length were less. The reasons were as follows: (1) The pressure drop was mainly dependent on the flow direction, and the pressure gradient in the *y*-direction experienced small changes inside the boundary layer in the entrance region only. (2) The change in buoyancy force was small because the density of water does not change significantly with temperature. The combined effect of these two factors resulted in a relatively stable and constant value for this force. Figure 20(b) indicates that the combined buoyancy and pressure gradient force increased along the tube length as the thermal boundary layer developed and the secondary flow strength increased. After the thermal boundary layer merged at $z/D = 60$ (Figure 12(b)), the combined buoyancy and pressure gradient force decreased slightly and reached an asymptotic value as the flow approached thermally fully developed flow.

As expected, Figure 20 indicates that the changes in the normalised forces increased with increasing Grashof number and occurred earlier along the tube length. An overall trend was that there were no significant changes in the forces after the hydrodynamic boundary layer merging point reached a maximum and the thermal boundary layer thickness became constant (thus, the flow became thermally fully developed).

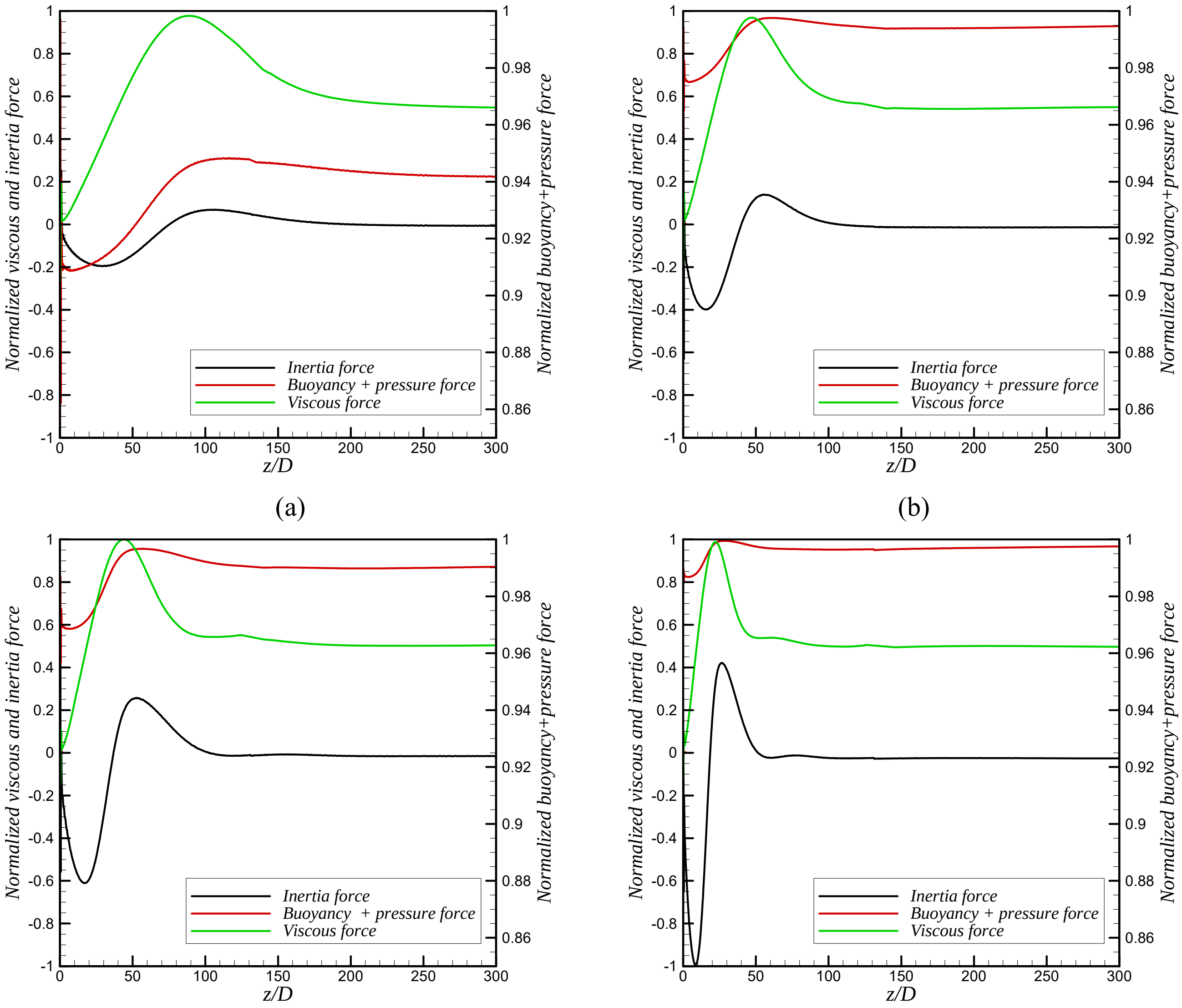

(a) (b)

(c) (d)

Figure 20: Development of the average inertia, combined buoyancy and pressure, and viscous forces in the momentum equation terms inside the hydrodynamic boundary layer in the *y*-direction from inlet for Grashof numbers of (a) 8.7×10^3 (Re = 1 800 and $\dot{q}$ = 1 kW/m^2), (b) 1.0×10^4 (Re = 1 000 and $\dot{q}$ = 1 kW/m^2), (c) 3.4×10^4 (Re = 1 800 and $\dot{q}$ = 3 kW/m^2) and (d) 5.5×10^4 (Re = 1 000 and $\dot{q}$ = 3 kW/m^2).

9.7 Summary

For mixed convective flow, it was concluded that the secondary flow strength and momentum forces in the boundary layer significantly influenced the temperature and velocity profiles and thus the development of the hydrodynamic and thermal boundary layers. These influences affected the local Nusselt numbers and caused the trend to be significantly different from forced convective flow.

From their experimental data, Meyer and Everts [2] identified three distinct regions in the local Nusselt numbers of developing flow: forced convection developing (FCD), mixed convection developing (MCD) and fully developed (FD). However, from the deeper insights obtained through the numerical investigation conducted in this study and considering the simultaneous development of the hydrodynamic and thermal boundary layers, i.e. in Figure 21, it was found that both the FCD and MCD regions could be divided into two separate regions. Furthermore, the flow became hydrodynamically fully developed after being thermally fully developed. Six different regions were therefore identified and defined as illustrated in Figure 21:

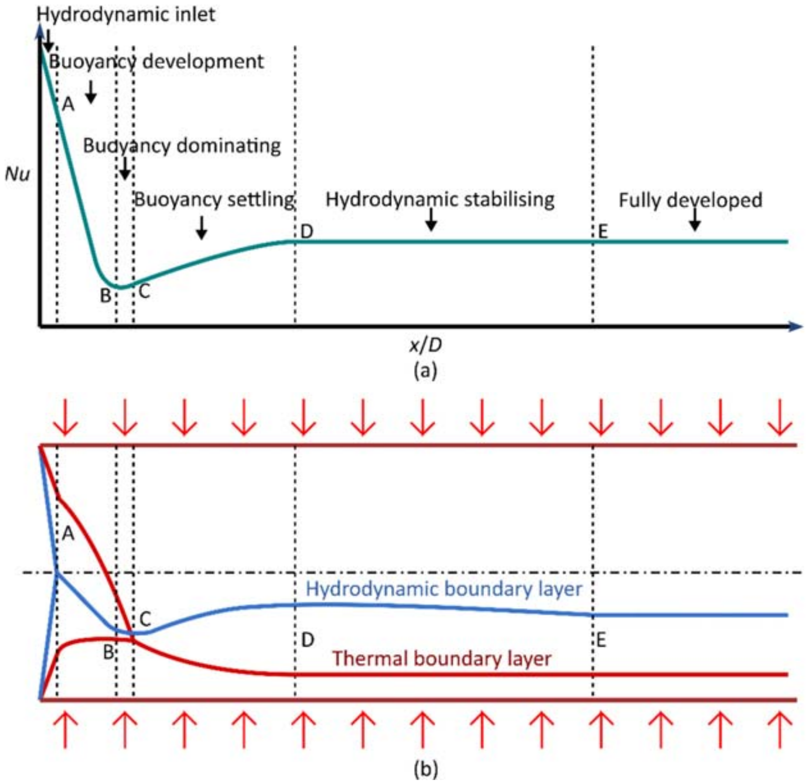

Figure 21: Schematic of the six different regions of simultaneously hydrodynamically and thermally developing mixed convective flow in terms of (a) the local Nusselt numbers along the tube length and (b) the hydrodynamic and thermal boundary layer development.

1. *Hydrodynamic inlet region* (0-*A*): Hydrodynamic and thermal boundary layers began forming in the radial direction from the inlet. The hydrodynamic boundary layer merged at Point *A*. Buoyancy effects were negligible in this region; therefore, similar to forced convection, it was only affected by Reynolds number, not Grashof number.
2. *Buoyancy development region* (*A-B)*: Buoyancy-induced secondary flow became sufficient to influence the development of the hydrodynamic and thermal boundary layers. The hydrodynamic boundary layer merging point shifted downwards, and the growth of the lower thermal boundary layer was suppressed, while the upper boundary layer thickness continued to increase. The secondary flow strength, viscous forces and combined buoyancy and pressure forces increased in this region. Point *B* corresponded to the following parameters: minimum Nusselt number, maximum secondary flow strength, and maximum viscous force. Because this region was significantly affected by the buoyancy-induced secondary flow, Point *B* occurred earlier with increasing Grashof number.
3. *Buoyancy dominating region* (*B–C*): Increased buoyancy effects along the tube length continued to shift the hydrodynamic boundary layer merging point towards the lower part of the tube, reaching a minimum thickness when the thermal boundary layer merged at Point *C*. This point also corresponded to the peaks in the inertia and combined buoyancy and pressure gradient forces. Furthermore, the buoyancy effects enhanced heat transfer compared with forced convection conditions and increased the local Nusselt numbers. Point *C* also occurred earlier with an increasing Grashof number.

4. *Buoyancy settling region* (*C-D*): The two symmetric secondary flow vortices caused the hydrodynamic boundary layer merging position to rise from its minimum (at Point *C*) to a maximum (at Point *D*). Furthermore, buoyancy effects and the presence of gravity led to the formation of a relatively stagnant high-temperature zone at the top of the tube, causing the merging point of the thermal boundary layer to move downwards along the tube length. Buoyancy-induced secondary flow continued to enhance heat transfer along the tube, but the gradient of the Nusselt numbers was less than in the dominating buoyancy region. The flow became thermally fully developed at Point *D*, which also occurred earlier with increasing Grashof number.
5. *Hydrodynamically stabilising region* (*D*–*E*): After the flow became thermally fully developed at Point *D*, there were no more changes in the thermal boundary layer thickness or the inertia, viscous, and combined buoyancy and pressure forces. The hydrodynamic boundary layer thickness approached an asymptotic value in this region and the flow became hydrodynamically fully developed at Point *E*. Contrary to the other points, point *E* occurred later with increasing Grashof number, as the flow took longer to stabilise.
6. *Fully developed region* (> *E*): The flow was hydrodynamically and thermally fully developed. Thus, the hydrodynamic and thermal boundary layer thicknesses and the Nusselt numbers remained constant along the tube length.

10 Conclusions

This study investigated the influence of buoyancy effects on developing the hydrodynamic and thermal boundary layers. Through analysing the fluid flow and heat transfer trends and focusing on the boundary layer and momentum development in the entrance region, this paper aimed to explain the unusual trends in the local mixed convective heat transfer coefficients compared with forced convective flow. Mixed convective flow through a circular tube with an inner diameter of 11.52 mm and a length of 9.5 m was simulated for different Grashof numbers, by varying the Reynolds number and heat flux, and the results were compared with experimental data. The long tube length was sufficient to ensure hydrodynamically and thermally fully developed flow before the exit of the tube. The numerical results were in very good agreement with the experimental data.

A new technique was developed to separate and evaluate three momentum terms regarding their fluid mechanics conceptions, including inertia, viscous and a combination of buoyancy and pressure gradient. Furthermore, a new non-dimensional parameter, namely the secondary flow strength, was defined for mixed convective flow. The development of hydrodynamic and thermal boundary layers was analysed using the conception of vorticity and velocity and temperature gradients.

The results showed that the rise in Nusselt number after its minimum was caused by secondary flow, being in its maximum at that location. Furthermore, an increase in Grashof number led to a decreased thermal entrance length, but an increased hydrodynamic entrance length. Considering the simultaneous development of the hydrodynamic and thermal boundary layers in the presence of secondary flow, six different regions were identified for developing mixed convective laminar flow.

The hydrodynamic boundary layer formed and merged in the *hydrodynamic inlet region*. In the *buoyancy development region*, buoyancy-induced secondary flow became sufficient to influence the development of the hydrodynamic and thermal boundary layers. The secondary flow strength, viscous forces and combined buoyancy and pressure forces increased in this region. Once the secondary flow strength and the viscous force reach a maximum at the start of the *buoyancy dominating region*, buoyancy effects were sufficient to enhance the heat transfer compared with that of forced convection conditions and increase the local Nusselt numbers. The inertia and combined buoyancy and pressure gradient forces reached a maximum at the end of the *buoyancy dominating region* and the width of this region decreased with increasing Grashof number. In the *buoyancy settling region*, the buoyancy-induced secondary flow continued to enhance heat transfer along the tube, but the gradient of the Nusselt numbers was less than in the *buoyancy dominating* region. The flow became thermally fully developed at the end of the *buoyancy settling region*. Thereafter, there were no more changes in the thermal boundary layer thickness or the inertia, viscous, and combined buoyancy and pressure forces, allowing the hydrodynamic boundary layer thickness to approach an asymptotic value and become hydrodynamically fully developed at the end of the *hydrodynamically stabilising region*. In the *fully developed region*, the flow was hydrodynamically and thermally fully developed. Thus, the hydrodynamic and thermal boundary layer thicknesses, as well as the Nusselt numbers remained constant along the tube length.

Acknowledgements

The funding obtained in South Africa from the National Research Foundation (Grant Number: 116623), Department of Science and Innovation (DSI), and the University of Pretoria is acknowledged and duly appreciated. They would additionally like to acknowledge the CHPC in Cape Town, South Africa, that made these simulations achievable.

Credit authorship contribution statement

Marilize Everts: conceptualisation, experiments, methodology, validation, formal analysis, investigation, project administration, writing: original draft**,** review and editing, funding acquisition.

Mostafa Mahdavi: methodology, CFD, validation, formal analysis, investigation, project administration, funding acquisition, writing: original draft**,** visualisation.

Josua Meyer: conceptualisation, resources, methodology, supervision, funding acquisition, writing: review and editing.

Mohsen Sharifpur: resources, supervision, review and editing.

Declaration of competing interest

The authors declared that there is no conflict of interest.

11 References

[1] D. Oliver, The effect of natural convection on viscous-flow heat transfer in horizontal tubes, Chemical Engineering Science, 17(5) (1962) 335-350.
[2] J.P. Meyer, M. Everts, Single-phase mixed convection of developing and fully developed flow in smooth horizontal circular tubes in the laminar and transitional flow regimes, International Journal of Heat and Mass Transfer, 117 (2018) 1251-1273.
[3] J.D. Jackson, M.A. Cotton, B.P. Axcell, Studies of mixed convection in vertical tubes, International Journal of Heat and Fluid Flow, 10(1) (1989) 2-15.
[4] W. Aung, Mixed Convection in Internal Flow, S. Kakaç, R.K. Shah, W. Aung (Eds.) Handbook of Single-Phase Convective Heat Transfer, John Wiley & Sons, New York, 1987, pp. 15.11-15.51.
[5] G.D. Raithby, K.G.T. Hollands, Natural Convection, W.M. Rohsenow, J.P. Hartnett, Y.I. Cho (Eds.) Handbook of Heat Transfer, McGraw-Hill, Boston, 1998, pp. 4.1-4.99.
[6] J.D. Jackson, M.A. Cotton, B.P. Axcell, Studies of mixed convection in vertical tubes, International Journal of Heat and Fluid Flow, 10(1) (1989) 1-15.
[7] J. Orfi, N. Galanis, C.T. Nguyen, Laminar fully developed incompressible flow with mixed convection in inclined tubes, International Journal of Numerical Methods for Heat & Fluid Flow, 3(4) (1993) 341-355.

[8] T. Maré, N. Galanis, S. Prétot, J. Miriel, Mixed convection with flow reversal in the entrance region of inclined tubes, International Journal of Numerical Methods for Heat & Fluid Flow, 15(7) (2005) 740-756.

[9] M. Everts, J.P. Meyer, Heat transfer of developing and fully developed flow in smooth horizontal tubes in the transitional flow regime, International Journal of Heat and Mass Transfer, 117 (2018) 1331-1351.

[10] M. Everts, J.P. Meyer, Relationship between pressure drop and heat transfer of developing and fully developed flow in smooth horizontal circular tubes in the laminar, transitional, quasi-turbulent and turbulent flow regimes, International Journal of Heat and Mass Transfer, 117 (2018) 1231-1250.

[11] M. Everts, J.P. Meyer, Flow regime maps for smooth horizontal tubes at a constant heat flux, International Journal of Heat and Mass Transfer, 117 (2018) 1274-1290.

[12] M. Everts, J.P. Meyer, Laminar hydrodynamic and thermal entrance lengths for simultaneously hydrodynamically and thermally developing forced and mixed convective flows in horizontal tubes, Experimental Thermal and Fluid Science, 118 (2020).

[13] M. Mahdavi, M. Sharifpur, J.P. Meyer, Discrete modelling of nanoparticles in mixed convection flows, Powder Technology, 338 (2018) 243-252.

[14] S. McComas, E. Eckert, Combined free and forced convection in a horizontal circular tube, Journal of Heat Transfer, 88(2) (1966) 147-152.

[15] R.L. Shannon, C.A. Depew, Combined free and forced laminar convection in a horizontal tube with a uniform heat flux, Journal of Heat Transfer, 90(3) (1968) 353-357.

[16] S.W. Hong, S.M. Morcos, A.E. Bergles, Analytical and experimental results for combined forced and free laminar convection in horizontal tubes, 5th International Heat Transfer Conference (IHTC-5), Tokyo, 1974, pp. 154-158.

[17] K.C. Cheng, J.W. Ou, Free convection effects on Graetz problem for large Prandtl number fluids in horizontal tubes with a uniform wall heat flux, 5th International Heat Transfer Conference (IHTC-5), Tokyo, Japan, 1974, pp. 159-163.

[18] G.S. Barozzi, E. Zanchini, M. Mariotti, Experimental investigation of combined forced and free convection in horizontal and inclined tubes, Meccanica, 20 (1985) 18-27.

[19] S. Piva, G.S. Barozzi, M.W. Collins, Combined convection and wall conduction effects in laminar pipe flow: numerical predictions and experimental validation under uniform wall heating, Heat and Mass Transfer, 30(6) (1995) 401-409.

[20] A.E. Bergles, R.R. Simonds, Combined forced and free convection for laminar flow in horizontal tubes with uniform heat flux, International Journal of Heat and Mass Transfer, 14(12) (1971) 1989-2000.

[21] J.P. Meyer, A.I. Bashir, M. Everts, Single-phase mixed convective heat transfer and pressure drop in the laminar and transitional flow regimes in smooth inclined tubes heated at a constant heat flux, Experimental Thermal and Fluid Science, 109 (2019).

[22] M. Everts, S. Bhattacharyya, A.I. Bashir, J.P. Meyer, Heat transfer characteristics of assisting and opposing laminar flow through a vertical circular tube at low Reynolds numbers, Applied Thermal Engineering, 179 (2020).

[23] K.C. Cheng, S.W. Hong, Combined free and forced laminar convection in inclined tubes, Applied Scientific Research, 27(1) (1973) 19-38.

[24] K.C. Cheng, S.W. Hong, G.J. Hwang, Buoyancy effects on laminar heat transfer in the thermal entrance region of horizontal rectangular channels with uniform wall heat flux for large Prandtl number fluid, International Journal of Heat and Mass Transfer, 15(10) (1972) 1819-1836.

[25] I.A. Hassanien, Combined forced and free convection in boundary layer flow of a micropolar fluid over a horizontal plate, Modelling, simulation & control. B, 58(1-2) (1995) 1-16.

[26] F.R. de Hoog, B. Laminger, R. Weiss, A numerical study of similarity solutions for combined forced and free convection, Acta Mechanica, 51(3-4) (1984) 139-149.

[27] H. Brauer, M. Dylag, J. Kasz, Heat transfer by combined free and forced convection in vertical tubes, Wärme- und Stoffübertragung, 23(2) (1988) 61-68.

[28] A. Muzzio, P. Parolini, Fully developed laminar mixed convection in uniformly heated pipes, Wärme- und Stoffübertragung, 29(8) (1994) 487-494.

[29] S.W. Hong, A.E. Bergles, Theoretical solutions for combined forced and free convection in horizontal tubes with temperature-dependent viscosity, Journal of Heat Transfer, 98(3) (1976) 459-465.

[30] R.L. Shannon, C.A. Depew, Forced laminar flow convection in a horizontal tube with variable viscosity and free-convection effects, Journal of Heat Transfer, 91(2) (1969) 251-258.

[31] P.H. Newell, Jr., A.E. Bergles, Analysis of combined free and forced convection for fully developed laminar flow in horizontal tubes, Journal of Heat Transfer, 92(1) (1970) 83-94.

[32] T.L. Bergman, A.S. Lavine, F.P. Incropera, D.P. De Witt, Fundamentals of Heat and Mass Transfer, 8th ed., Wiley, New York, 2017.

[33] Y.A. Cengel, A.J. Ghajar, Heat and Mass Transfer: Fundamentals and Applications, 5th ed., McGraw-Hill, 2015.

[34] A. Bejan, Convection Heat Transfer, 4th ed., John Wiley & Sons, Hoboken, 2013.

[35] A. Sharma, Introduction to computational fluid dynamics : development, application and analysis, John Wiley & Sons Ltd, Chichester, 2017.

[36] D.-Y. Shang, L.-C. Zhong, Heat Transfer of Laminar Mixed Convection of Liquid, 1 ed., Springer International Pubmishing, Switzerland, 2016.

[37] H.A. Mohammed, Y.K. Salman, Combined convection heat transfer for thermally developing aiding flow in an inclined circular cylinder with constant heat flux, Applied Thermal Engineering, 27(8-9) (2007) 1236-1247.

[38] S.M. Morcos, A.E. Bergles, Experimental investigation of combined forced and free laminar convection in horizontal tubes, Journal of Heat Transfer, 97(2) (1975) 212-219.

[39] M. Everts, J.P. Meyer, Test Sections for Heat Transfer and Pressure Drop Measurements: Construction, Calibration, and Validation, J.P. Meyer, M. De Paepe (Eds.) The Art of Measuring in the Thermal Sciences, CRC Press, Boca Raton, 2021, pp. 107-158.

[40] G. Maranzana, I. Perry, D. Maillet, Mini- and micro-channels: influence of axial conduction in the walls, International Journal of Heat and Mass Transfer, 47(17) (2004) 3993-4004.

[41] A. Bakker, R.D. LaRoche, E.M. Marshall, Laminar flow in static mixers with helical elements, The Online CFM Book, 2000.

[42] C.O. Popiel, J. Wojtkowiak, Simple formulas for thermophysical properties of liquid water for heat transfer calculations [from O°C to 150°C], Heat Transfer Engineering, 19(3) (1998) 87-101.

[43] Ansys, Ansys Fluent 19.3 Theory Guide, Ansys Inc., 2019.

[44] M. Everts, Single-phase mixed convection of developing and fully developed flow in smooth horizontal circular tubes in the laminar, transitional, quasi-turbulent and turbulent flow regimes, PhD thesis, University of Pretoria, Pretoria, 2017.

[45] R.K. Shah, A.L. London, Laminar Flow Forced Convection in Ducts, Academic Press, New York, 1978.